Conductive Channels in the Deep Oceanic Lithosphere Could Consist of Garnet Pyroxenites at the Fossilized Lithosphere–Asthenosphere Boundary

Thomas P. Ferrand

minerals

MDPI

Article

Conductive Channels in the Deep Oceanic Lithosphere Could Consist of Garnet Pyroxenites at the Fossilized Lithosphere–Asthenosphere Boundary

Thomas P. Ferrand

Institut des Sciences de la Terre d'Orléans, Université d'Orléans—CNRS UMR-7327, 45100 Orléans, France; thomas.ferrand@univ-orleans.fr

Received: 10 November 2020; Accepted: 8 December 2020; Published: 10 December 2020

Abstract: Magnetotelluric (MT) surveys have identified anisotropic conductive anomalies in the mantle of the Cocos and Nazca oceanic plates, respectively, offshore Nicaragua and in the eastern neighborhood of the East Pacific Rise (EPR). Both the origin and nature of these anomalies are controversial as well as their role in plate tectonics. The high electrical conductivity has been hypothesized to originate from partial melting and melt pooling at the lithosphere–asthenosphere boundary (LAB). The anisotropic nature of the anomaly likely highlights high-conductivity channels in the spreading direction, which could be further interpreted as the persistence of a stable liquid silicate throughout the whole oceanic cycle, on which the lithospheric plates would slide by shearing. However, considering minor hydration, some mantle minerals can be as conductive as silicate melts. Here I show that the observed electrical anomaly offshore Nicaragua does not correlate with the LAB but instead with the top of the garnet stability field and that garnet networks suffice to explain the reported conductivity values. I further propose that this anomaly actually corresponds to the fossilized trace of the early-stage LAB that formed near the EPR about 23 million years ago. Melt-bearing channels and/or pyroxenite underplating at the bottom of the young Cocos plate would transform into garnet-rich pyroxenites with decreasing temperature, forming solid-state high-conductivity channels between 40 and 65 km depth (1.25–1.9 GPa, 1000–1100 °C), consistently with experimental petrology.

Keywords: tectonics; mantle; East Pacific Rise; Nicaragua; high-conductivity channels; magnetotellurics; garnet; melt; hydrogarnet; pyrope; lithosphere; conductivity

1. Introduction

A MT experiment identified an off-axis conductive asthenosphere at 60–120 km depth beneath a resistive lithosphere at the southern EPR spreading ridge [1,2]. The conductive anomaly has been interpreted as due to partial melting in the asthenosphere (Figure 1a) [1]. A similar electrical anomaly was identified offshore Nicaragua (Figure 1b) [3]. Based on similar activity and the spreading rate of the southern and northern EPR, it is reasonable to assume that equivalent ridge processes are occurring for the Cocos and Nazca plates [3]. Both anomalies are highly anisotropic (Figure 1) [1,3], exhibiting significantly larger conductivity values reported either in the spreading direction [1] or in the subduction direction [3], which exhibit a ≈15° angle offshore Nicaragua. The observed anisotropy has been interpreted as due to melt channels forming in the shearing direction at the base of the oceanic plate [4], likely parallel to the volcanoes' alignments, indicated on the geological map (Figure 2).

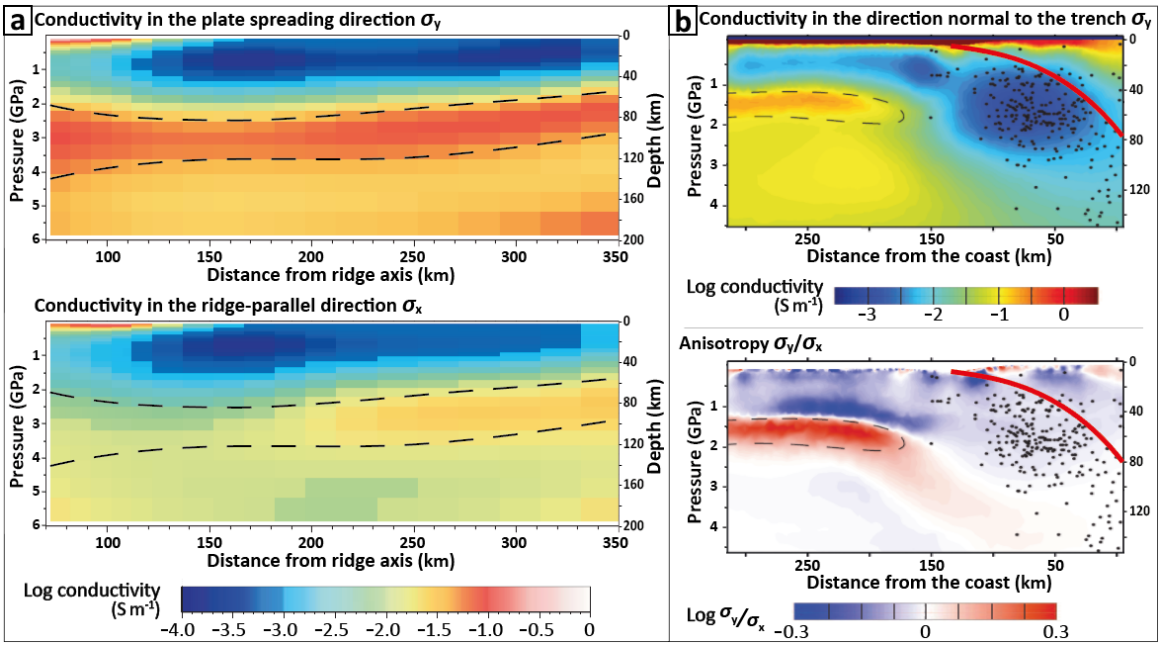

Figure 1. High-conductivity channels at the bottom of the Nazca and Cocos Plates. Comparison between two MT profiles showing anisotropic high-conductivity features below the Nazca Plate ((**a**) east of the EPR, 3–6 Ma) [1] and within the Cocos Plate ((**b**) offshore Nicaragua; 22–25 Ma) [3]. For the young Nazca Plate (**a**), the conductivity reaches only $\sim 8 \times 10^{-2}$ S·m^{-1} in the spreading direction (σ_y) and σ_y/σ_x reaches ≈10; for the old portion of the Cocos Plate (**b**), the conductivity reaches up to $\sim 2 \times 10^{-1}$ S·m^{-1} in the direction normal to the trench (σ_y) and σ_y/σ_x ≈2. The dashed black lines locate the anomaly and highlight its anisotropic nature. The thick red line (**b**) corresponds to the subduction interface.

Because silicate melts are significantly more conductive than silicate minerals (e.g., [5]), the high electrical conductivity has been hypothesized to originate from partial melting in the asthenosphere (1400 °C on average) [6] and melt pooling at the LAB (≈1300 °C) [1,3,4,7,8]. However, it is not clear how a silicate melt could remain stable at the bottom of the oceanic plate for millions of years, notably considering plate cooling [9,10]. The melt should continuously percolate from the asthenosphere [11]. Yet, most of the hydrous melt should have been emplaced at or near the ridge axis, as pointed by previous studies, e.g., [1,3].

Preferred partitioning of water into silicate melts may induce significantly higher water contents due to deep grain-boundary percolation [12] especially in the case of deep intraplate melting associated with small-scale convection [13]. The hydrous melt would then collect beneath the colder lithosphere, which is less permeable [14], and large-scale asthenospheric flow [15] would induce melt shearing into a network of interconnected melt bands preferentially aligned in the spreading direction, e.g., flow-aligned tube-like structures [16], as suggested by experimental studies [17]. The latter is in good agreement with the existence of stress gradients normal to the shear direction [4], hypothesized to explain the anisotropy of the electrical anomalies [1,3]. Regarding the young Cocos plate close to the EPR (<5 Ma), this is well supported and reasonable [1,4], but this is definitely not the case offshore Nicaragua [18], as detailed hereinafter.

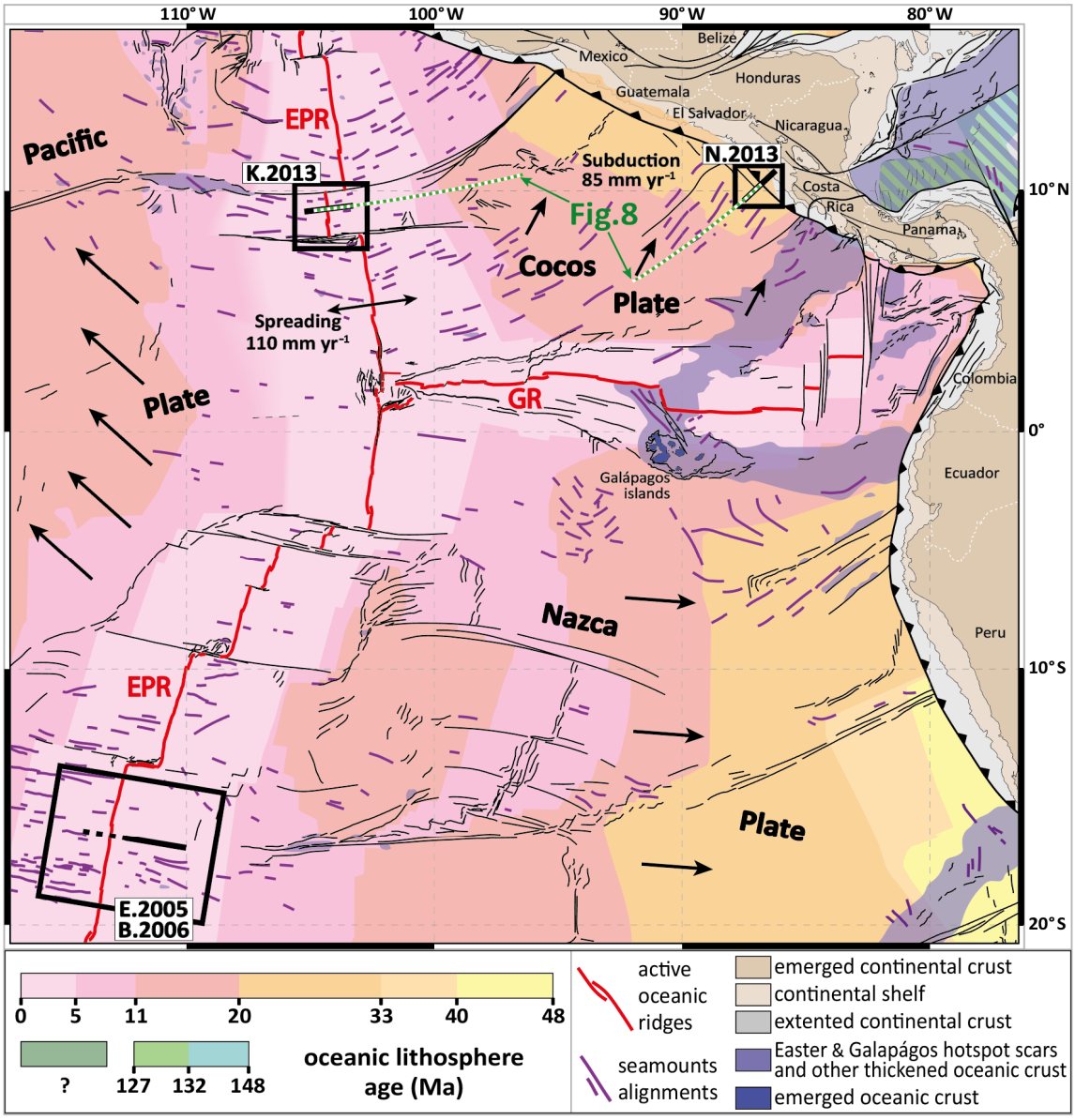

Figure 2. Synthetic map of the Eastern Pacific Ocean. Simplified map built from [19,20] and Google Earth. The spreading rate at the EPR is estimated to 11 cm·yr^{-1} for the Cocos Plate [21] and 10–15 cm·yr^{-1} for the Nazca Plate [22]. Large black arrows indicate plate motion direction. MT surveys: EPR = East Pacific Rise; GR = Galápagos Ridge. References: B.2006 = [2]; E.2005 = [1]; K.2013 = [21]; N.2013 = [3].

Some studies further argue that the LAB beneath young plates (<25 Ma) would consist of a thin, partially molten, layer of low viscosity that would decouple the overlying brittle lithosphere from the deeper convecting mantle [3]. Consequently, it has been interpreted that the presence of melt was durable at depth over millions of years [23]. Furthermore, it has been speculated that the thickness of the anisotropic high-conductivity layer inferred by MT data offshore Nicaragua would correspond to a 30-km-thick melt layer [3]. Mantle-derived melts are stable at these depths in a warm damp mantle [4], which has led to postulate that the temperature of the anomaly offshore Nicaragua was >1400 °C [23], although plate cooling models rather predict 1000–1100 °C [14]. In other words, even though the LAB is located around 80 km depth (typical lithospheric thickness with an age of 20–25 Ma [14]), several studies have considered that it was located around 40 km [3,18,23], which is physically impossible.

With this paper, I add a petrological point of view to the discussion in order to highlight that melt-free scenarios exist and may be more reasonable. I propose to investigate the nature of the anisotropic conductive anomaly offshore Nicaragua, through a global understanding of the structure of the Cocos plate. If the anomaly offshore Nicaragua is effectively the consequence of melt pooling at the LAB, then it consists of a fossilized LAB, in which the melt would have solidified. Mantle-derived melts should crystallize into aggregates rich in pyroxenes and garnet [24,25], as illustrated on the P-T diagram (Figure 3a), in which I compare garnet stability to partial melting conditions according to experimental studies (Figure 3b). Garnet, known to be connected in natural mantle xenoliths, e.g., [26] (Figure 4a), has been evidenced experimentally to reach conductivity values as high as 10^{-1} S·m^{-1} [27–29] due to the combined effect of iron in both dodecahedral (Fe^{2+}) and octahedral (Fe^{3+}) sites and hydrogarnet substitution (4 H^{+} instead of Si^{4+}) in tetrahedral sites (Figure 4b). According to thermodynamics (Figure 3a), plate cooling should lead to the transformation of spinel-bearing pyroxenites into garnet pyroxenites, localizing garnet crystals at the reaction front, i.e., at grain boundaries (Figure 4c). This brings us to the question: could the conductive channels offshore Nicaragua consist of networks of conductive minerals such as garnet?

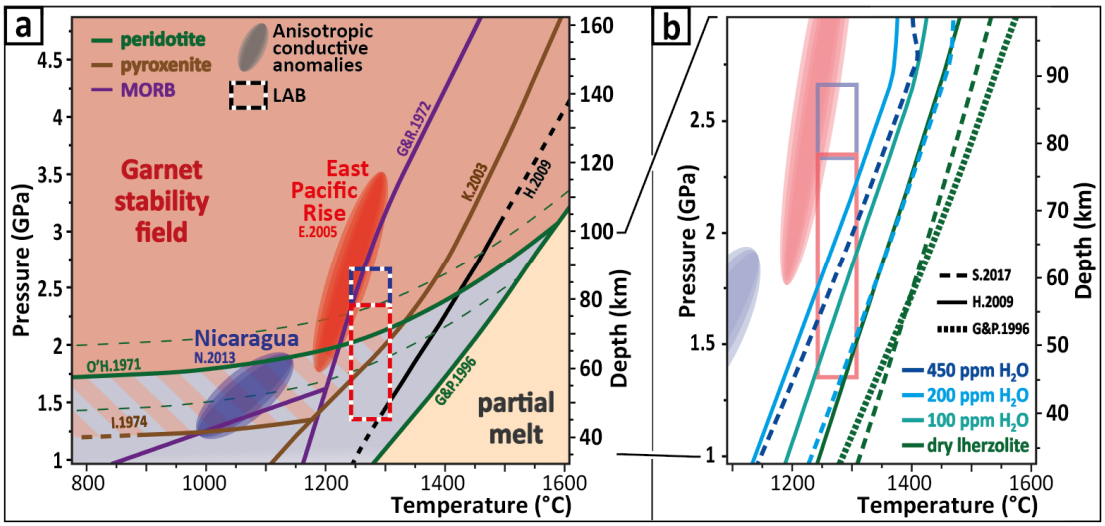

Figure 3. Correlation between electrical anomalies and garnet stability in mantle rocks. (**a**) Phase diagram showing the P-T conditions for the electrical anomalies offshore Nicaragua (dark blue) [3] and near the EPR (light red) [1] in accordance with Figure 1. (**b**) Impact of water content on the solidus (i.e., onset of melting) of lherzolite (i.e., fertile peridotite). In both (**a**) and (**b**), P-T conditions at the LAB are also indicated for comparison (dark blue and light red boxes). Solidus from [30] are extrapolated for temperatures between 1100 and 1300 °C (plain lines). References: E.2005 = [1]; H.2009 = [30]; G&P.1996 = [31]; G&R.1972 = [32]; I.1974 = [33]; K.2003 = [34]; N.2013 = [3]; O.1971 = [35]; S.2017 = [36].

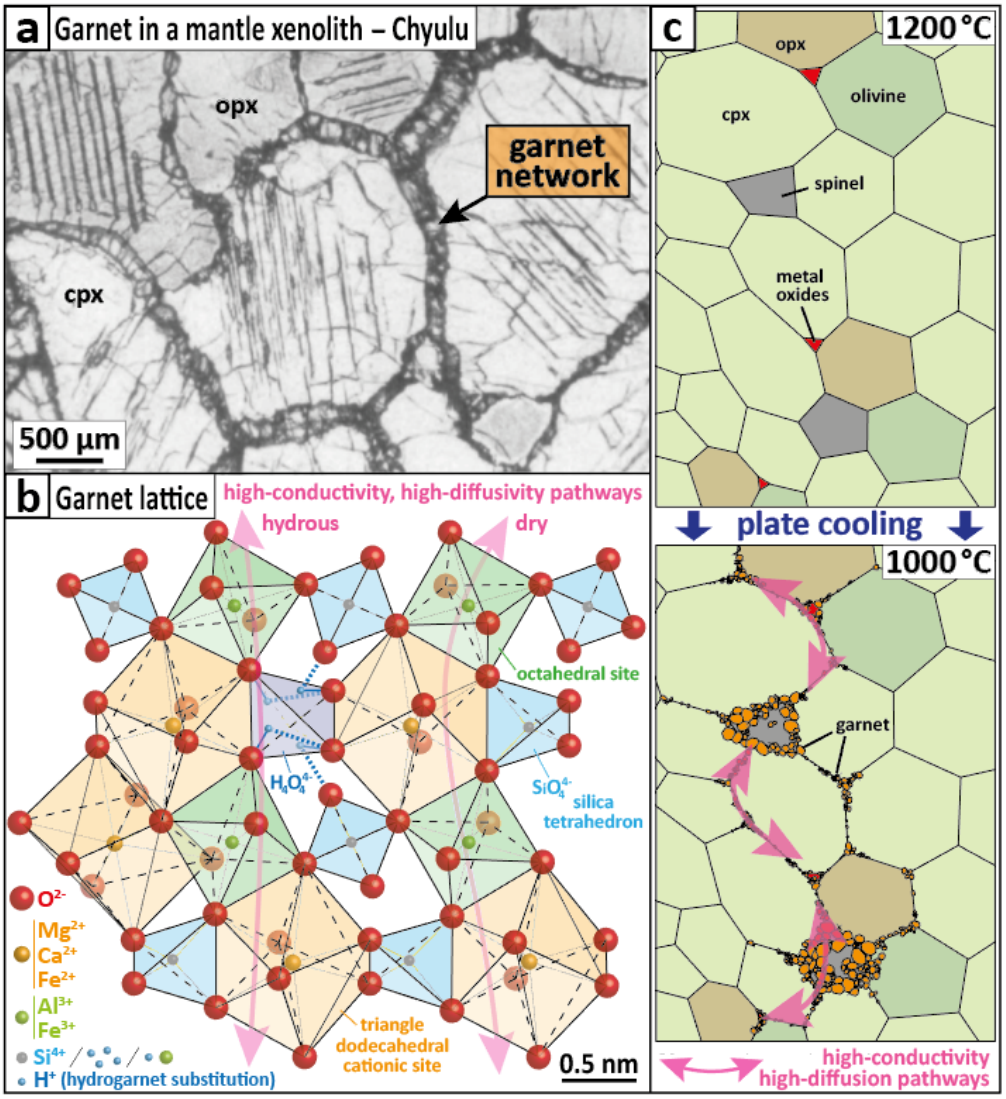

Figure 4. Garnet as a conductive phase in the mantle. (**a**) Natural garnet network in a mantle xenolith from Chyulu, Southern Kenya [26]. (**b**) Portion of the garnet structure (adapted from [37]) illustrating the effect of hydrogarnet substitution [38], stabilized by hydrogen bonding [39], on electron pathways (pink). (**c**) Schematics of an example of the formation of a garnet network through a metamorphic reaction at grain boundaries at 2–3 GPa in a pyroxenite due to progressive plate cooling. As temperature decreases from 1200 to 1000 °C, garnet networks can organize in pyroxene-rich zones, which could explain the conductivity anomaly offshore Nicaragua.

2. Methods

2.1. Confrontation of Studies on Natural and Experimental Systems

This study is based on a detailed analysis of the literature about anisotropic high-conductivity anomalies evidenced with MT (e.g., [1–3,21]) in light of experimental studies on electrical conductivity (e.g., [4,28,29,40]), thermodynamics (e.g., [33–35,41]) and rheology (e.g., [17,42]), along with numerical modeling (e.g., [7,43–45]) and field geology [46–49].

A summary of conductivity values for minerals typical of the upper mantle is provided in Figure 5. The connectivity of these phases is key in the control of the bulk conductivity, as illustrated in Figure 6 and explained in detail in Section 2.2.

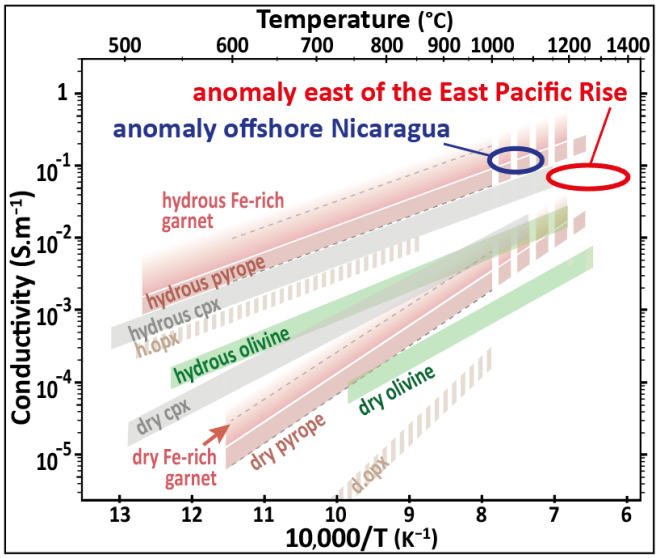

Figure 5. Conductivity of major mantle minerals and impact of hydration. Electrical conductivity versus reciprocal temperature for olivine, clinopyroxenes and garnets. The green, gray, red and hatched brown shades correspond to electrical conductivity values for dry olivine (X_{Fe} = 0.1) [50], hydrous olivine (465 ppm H_2O) [51], dry and hydrous (375 ppm H_2O) clinopyroxene [52], dry and hydrous (465 ppm H_2O) pyrope (Py_{73}-Alm_{14}-Grs_{13}, 2 GPa) [28] and dry and hydrous (200 ppm H_2O) orthopyroxene [40].

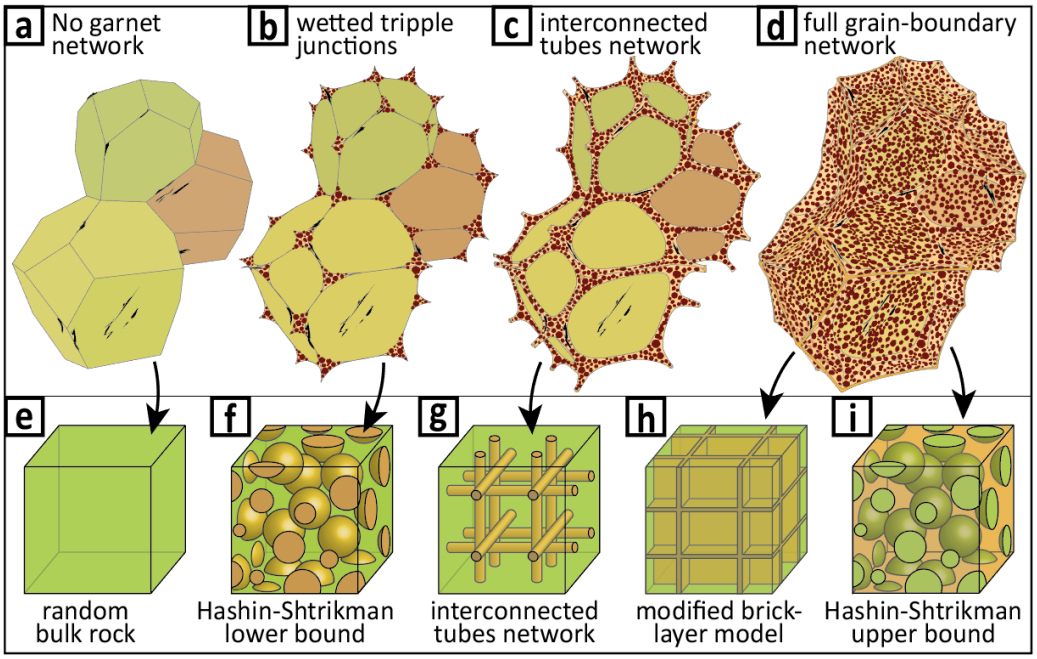

Figure 6. Representation of the different physical models used for electrical conductivity simulations. Sketches of the grains with variable geometries of the garnet networks (**a**–**d**) and corresponding simplified geometries used for the physical models (**e**–**i**) presented in Figure 7. Drawings (**a**,**b**,**d**) were adapted from case (**c**), inspired from [53]. Garnet is represented in dark red, and possible local graphite impurities are represented in black.

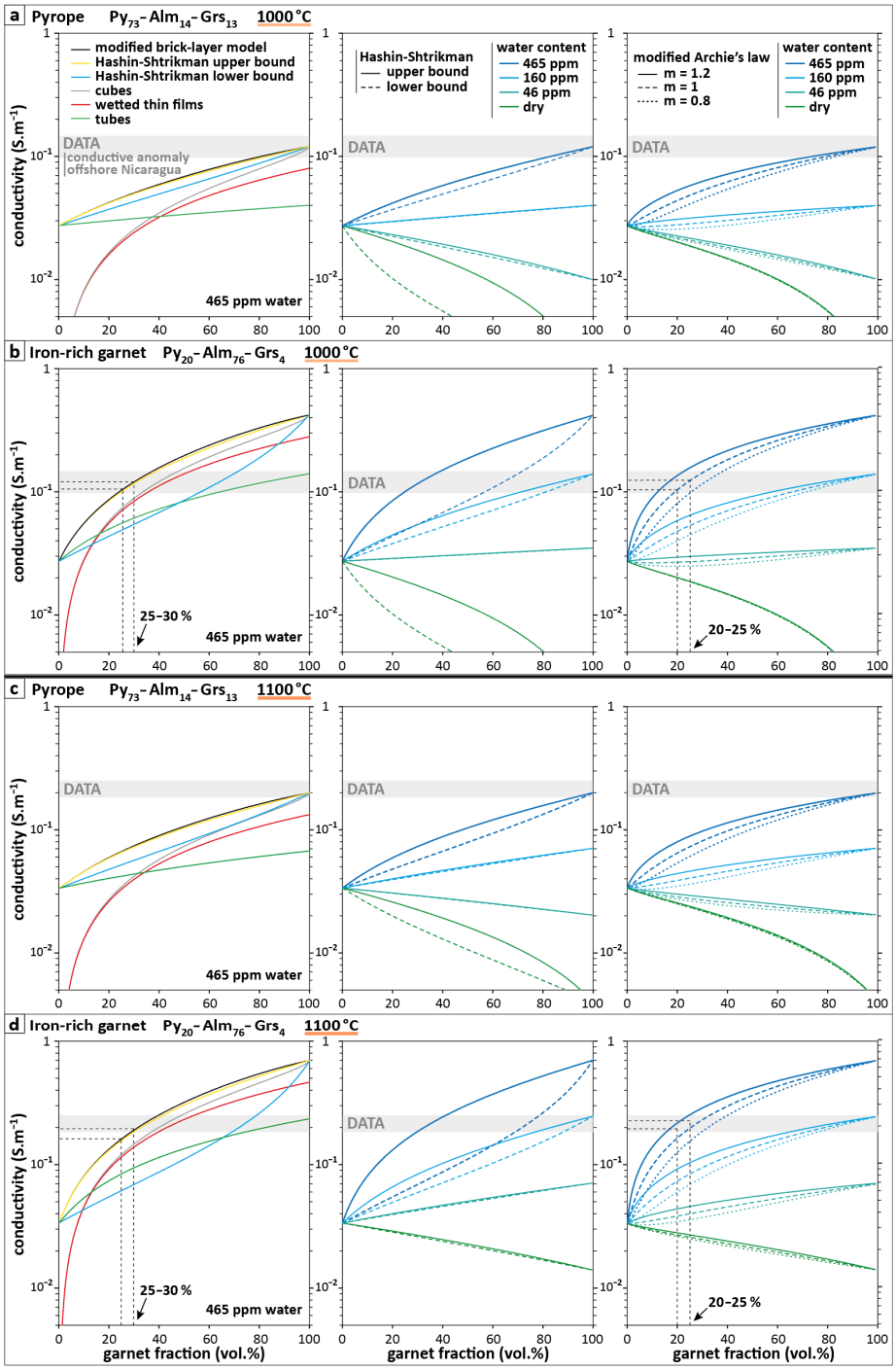

Figure 7. Numerical simulations of electrical conductivity for various amounts of garnet. Physical models illustrated in Figure 6 and additional modeling with a modified Archie's law [54] (implicit geometrical factors). The formulas are described in Table 1. The simulations are performed for a pyroxenite at 2 GPa (≈60 km) containing (**a**) natural pyrope at 1000 °C, (**b**) iron-rich garnet at 1000 °C, (**c**) natural pyrope at 1100 °C and (**d**) iron-rich garnet at 1100 °C. In each case, three subfigures are presented, showing simulation results for the different models (left), for the Hashin–Shtrikman upper and lower bounds (center) and the modified Archie's law (right). The gray shade indicates the data (conductive anomaly recorded using MT offshore Nicaragua) [3]. The high impact of water content is illustrated for the Hashin–Shtrikman geometry and Archie's law. The impact of water defects on the conductivity of olivine and pyroxenes (values and references in Figure 5) is taken into account (except for the "wetted thin films" and "cubes" models, too simplified if both the conductive network and the less conductive part of the rock are somehow conductive).

Table 1. Various models to compute electrical conductivity in Figure 7.

Models	Formula	References
Hashin–Shtrikman upper bound	$\sigma^* = \sigma_n + \frac{1-x_n}{\frac{1}{\sigma_b-\sigma_n}+\frac{x_n}{3\sigma_n}}$	[55]
Hashin–Shtrikman lower bound	$\sigma^* = \sigma_b + \frac{1-x_n}{\frac{1}{\sigma_n-\sigma_b}+\frac{1-x_n}{3\sigma_n}}$	
Tubes model	$\sigma^* = \frac{1}{3}X_n\sigma_n + (1-x_n)\sigma_b$	[56]
Wetted thin films model	$\sigma^* = \frac{\sigma_b\sigma_n(1-x_n)^{\frac{2}{3}}}{\sigma_n(1-x_n)^{\frac{1}{3}}+\sigma_b\left[1-(1-x_n)^{\frac{1}{3}}\right]} + \sigma_n\left[1-(1-x_n)^{\frac{2}{3}}\right]$	[57]
Modified brick-layer model	$\sigma^* = \frac{\sigma_n\left[\sigma_n\left((1-x_n)^{\frac{2}{3}}-1\right)-\sigma_n(1-x_n)^{\frac{2}{3}}\right]}{\sigma_b\left[(1-x_n)-(1-x_n)^{\frac{2}{3}}\right]+\sigma_n\left[(1-x_n)^{\frac{2}{3}}+x_n-2\right]}$	[58]
Modified Archie's law	$\sigma^* = \sigma_b(1-x_n)^p + \sigma_n {x_n}^m$ $p = \frac{\log(1-{x_n}^m)}{\log(1-x_n)}$	[54]

2.2. Modeling of the Electrical Conductivity

In the following, I merge the knowledge from different disciplines of Earth Sciences in order to propose a fully consistent explanation for the high-conductivity anomalies in the Cocos plate and discuss the limitations of alternative models. The bulk electrical conductivity of a multiphase system is controlled by the interconnection of conductive phases and the topology of the conductive network, e.g., [54,59,60]. In this study, I consider a conductive garnet network within a mantle pyroxenite, typical of the mantle beneath magma-rich spreading centers.

To compute the bulk conductivity of the host rock, I consider a random distribution of phases. For N phases of conductivity σ_i and fraction x_i, the random model gives a bulk conductivity σ^* as follows:

$$\sigma^* = \prod_{i=1}^{N} {\sigma_i}^{X_i}$$

In order to predict the bulk conductivity of rocks as a function of an interconnected conductive phase, typically partial melt or saline fluid, connectivity models have been developed (e.g., [54,61]) and references therein. Connectivity problems can be solved using the percolation theory [62]. The connectivity threshold is a function of the geometry of the conductive network, e.g., [59]. In this study, even though the conductive network consists of a solid phase, I consider a geometry that is analogous to the melt networks analyzed by [12,59]. To account for the impact of garnet pyroxenites and especially garnet connectivity on the bulk electrical conductivity, I consider various network geometries [55–58], detailed in Table 1 and illustrated in Figure 6, that I compare with a modified Archie's law [54] (see next paragraph). The conductivity values used in the modeling (Table 2) are obtained from experimental works on each phase [28,29,40,50–52]. Moderate water contents are considered, consistent with the literature [63,64]. The impact of water on garnet conductivity (Figure 5), and thus on bulk conductivity, appears clearly in Figure 7.

Table 2. Parameters used for electrical conductivity simulations.

	Pyroxenite Composition				
	Olivine	**cpx**	**opx**	**Garnet**	**Connectivity of Garnet**
No garnet	10%	80%	10%	0%	no
10% garnet	9%	72%	9%	10%	yes
20% garnet	8%	64%	8%	20%	
	Water Content				
	Olivine	**cpx**	**opx**	**Garnet**	
	20 ppm	375 ppm	200 ppm	0–465 ppm	

	Corresponding Conductivity ($S \cdot m^{-1}$)					
Temperature	**Olivine**	**cpx**	**opx ***		**pyrope**	**Fe-Rich Garnet**
1000 °C	1.8×10^{-3}	4×10^{-2}	2×10^{-2}	dry	1.3×10^{-3}	1.3×10^{-3}
				46 ppm H_2O	1.0×10^{-2}	3.5×10^{-2}
				160 ppm H_2O	4.0×10^{-2}	1.4×10^{-1}
				465 ppm H_2O	1.2×10^{-1}	4.2×10^{-1}
1100 °C	2×10^{-3}	5×10^{-2}	3×10^{-2}	dry	4.0×10^{-3}	1.4×10^{-2}
				46 ppm H_2O	1.8×10^{-2}	7.0×10^{-2}
				160 ppm H_2O	7.0×10^{-2}	2.5×10^{-1}
				465 ppm H_2O	2.0×10^{-1}	7.0×10^{-1}
references	[51]	[52]	[40]		[28,29]	

Simulated rocks consist of olivine, clinopyroxene (cpx), orthopyroxene (opx) and garnet (pyrope or Fe-rich garnet). *conductivity values for 200 ppm H_2O and X_{Fe} = 0.1 [40]; some more H_2O and less Fe would increase and decrease the conductivity, respectively.

Archie's law [65] is commonly used to compute bulk conductivity relying only on knowledge of the conductive phase and its network geometry. The value of the exponent *m* in Archie's law implicitly contains the effective connectivity of the conductive phase. A modified form of the expression accounts for the conductivity of both relatively conductive and relatively resistive phases [54] (Table 1). Such a modified Archie's law is relevant to interpret bulk conductivity values as a function of conductor fraction [59].

As illustrated in Figure 7, considering moderate garnet hydration (discussed in Section 4.3.1), a conductive network of about 20–25 vol.% reproduces MT observations. Regarding the geometry of the garnet network, it appears that both the Hashin–Shtrikman upper bound and the modified brick-layer models provide simulations that best fit the data (Figure 7). In order to put it back in context, I drew Figure 8 based on published studies on the EPR [21], the MELT region east of the EPR (Nazca Plate) [1] and the anomaly offshore Nicaragua [3]. Assuming that the conductive features are representative of the Cocos and Nazca Plates and oceanic plates in general, the full cross-section of the Cocos plate is shown in Figure 8a. The electrical conductivity profiles (Figure 8a,b) are drawn using a unified color scale from the profiles presented in Figure 1. In Figure 8c, I propose a tectonic and petrological interpretation of the synthetic electrical conductivity profile presented in Figure 8b. The profiles are explained in Section 3 and discussed in Section 4.

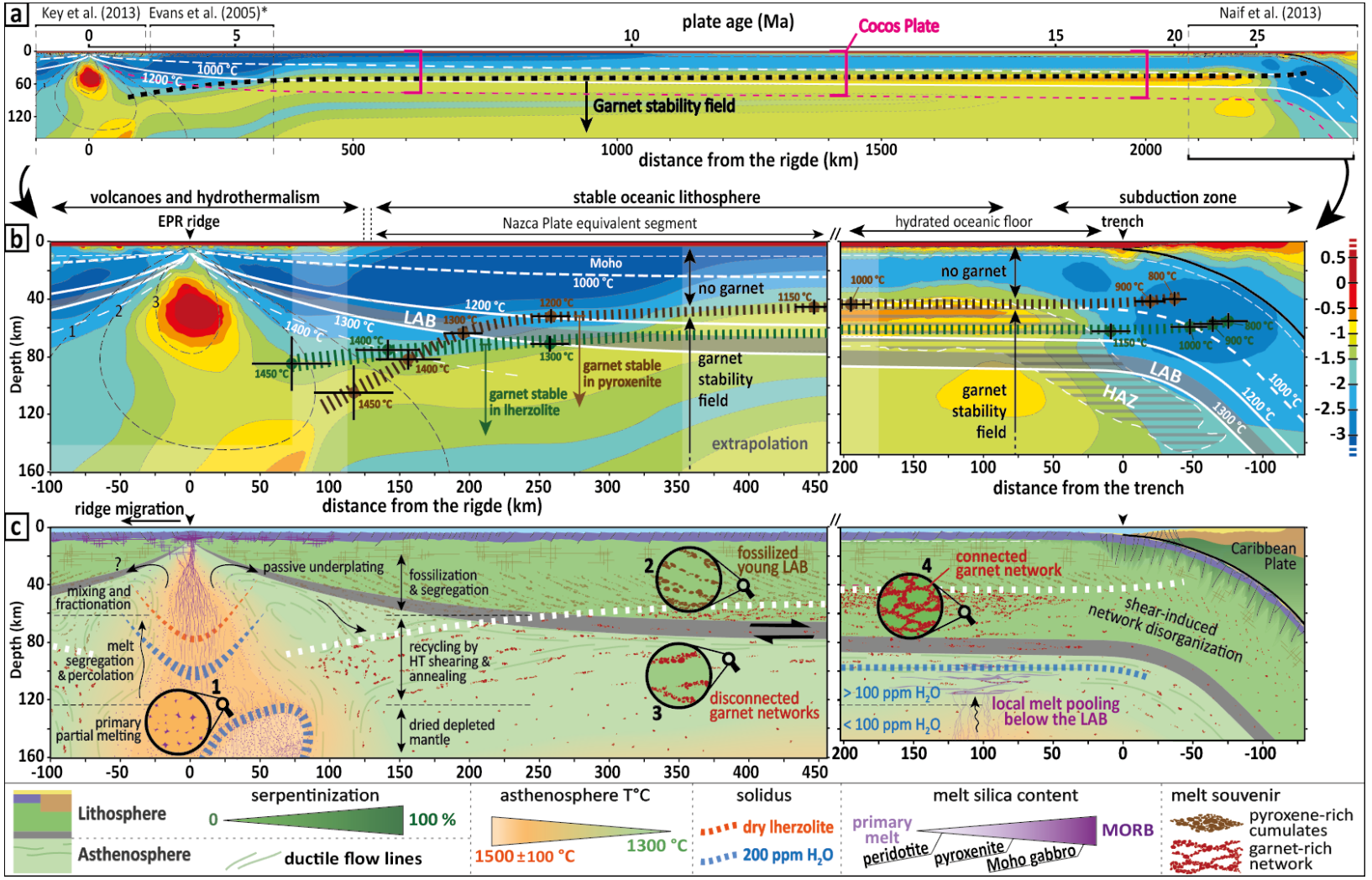

Figure 8. Synthetic cross-section of the Cocos Plate showing the electrical conductivity in the spreading direction, including an equivalent segment from the Nazca Plate. (**a**) Overview of the electrical structure of the Cocos plate from the EPR to the subduction offshore Nicaragua. (**b**) Focus on the youngest portion (EPR) [21] with

extrapolation * from the Nazca Plate [1] and the oldest portion (subduction) [3]. The hatched lines indicate the depth at which garnet becomes stable in the case of a peridotite (green) and the case of a pyroxenite (brown). The gray dashed lines (beneath EPR) account for melt ascent calculations [21] in cm·yr^{-1}. (**c**) Geological interpretation based on a review of knowledge up to date (details in Section 4) notably highlighting that conductive minerals could explain the electrical anomalies and that melting is not required. From partial melting beneath the EPR (1), upward segregation, mixing and fractionation lead to passive underplating of pyroxene-rich cumulates and/or intergranular glass intrusions, i.e., fossilized early-stage LAB (2), whereas garnet is stable at higher pressures (3). Furthermore, plate cooling with age [9] leads to the transformation [66] of the refertilized mantle and the formation of garnet-rich connected networks (4). The question mark indicates the interrogation regarding the asymmetry of the electrical anomaly, i.e., ridge migration (discussion in Section 4). Asthenosphere flow lines are adapted from [44]. The thickness of the oceanic crust is ≈7 km on average [67], and the cross-section of Nicaragua is inspired from [68]. * The MT profile from [1] was acquired on another segment of the EPR, i.e., the MELT area, located in Figure 2, between the Pacific and Nazca plates (see discussion in Section 4). In this representation, the LAB is between the 1260 °C and 1300 °C isotherms (Section 3.1), which is a matter of discussion (Section 4.3.4). Legend: LAB = lithosphere–asthenosphere boundary; HAZ = high-anisotropy zone [3].

3. Results

3.1. The Anisotropic Anomaly Cannot Be the LAB

Studies have argued that the anisotropic high-conductivity anomalies east of the EPR and offshore Nicaragua are due to the same phenomenon [3,23]. The electrical anomalies would be due to melt pooling at the LAB [8,16], which is relatively well established for the anomaly detected near the EPR [1]. However, regarding the anomaly offshore Nicaragua [3], plate cooling [9,10] should lead to a much thicker lithosphere, as illustrated in Figure 8 and detailed hereafter. As the EPR is a fast-spreading center, the lithospheric thickness in its vicinity increases rapidly, from 30 ± 5 km at 1 Ma to 65 ± 5 km at ≈6 Ma [9]. Considering the large-scale symmetry between the Cocos and Pacific lithospheres, respectively located on the western and eastern sides of the EPR (Figure 2), the oldest portion of the Cocos Plate offshore Nicaragua (23–24 Ma) should be 85 ± 5 km thick [10]. It should be noted that the lithosphere thickness is defined here by the thermal definition of the lithosphere (discussion in Section 4.3.4). In Figure 8, the LAB is represented between the isotherms 1260 °C and 1300 °C, based on a relative symmetry of the deep lithospheric structure around the EPR. Tomography models tend to favor a rheological definition of the lithosphere and provide lower estimates for the lithospheric thickness, e.g., 45–54 km for a plate age of 20–25 Ma with a lower temperature of 1150–1200 °C [69].

The abnormally shallow location of the conductive anomaly relative to the expected thickness of the lithosphere has already been pointed out in a previous study [18]. The discrepancy has been hypothesized to originate from plate-bending-induced decompressional melting [18], but if such a phenomenon existed, it should be observed anywhere a young plate (<25 Ma) enters a subduction zone. In addition, decompressional melting due to plate bending, if any, should not induce high conductivity in the spreading direction but the trench direction. In addition, if such bending-induced decompressional melting were realistic, it would be observed in other subduction zones of the same age or younger, with associated volcanism. Importantly, I recall that the volcanoes' alignments highlighted in Figure 2 do not consist of active volcanoes as the volcanic activity is limited to the vicinity of oceanic ridges [46,47,70,71].

3.2. The Anomaly Correlates with the Top of the Garnet Stability Field

Comparing the solidus of dry peridotites [31], pyroxenites [34] and mid-oceanic-ridge basalts (MORB) [32,72], and considering significant hydration [30,36], it is confirmed that partial melting is compatible with the P-T conditions at the LAB of both the young [1] and old [3] plates (Figure 3). Interestingly, partial melting is not fully compatible with the P-T conditions corresponding to the electrical anomalies. In particular, the anomaly offshore Nicaragua (1.25–1.9 GPa, 1000–1100 °C) is incompatible with the stability of mantle-derived melt (Figure 3). Instead, there is a correlation between the high-conductivity feature and the stability of garnet pyroxenite [33] in the deep Cocos lithosphere (Figure 3a).

Taking into account that the anisotropic high-conductivity anomaly offshore Nicaragua does not correspond to the LAB but a much colder feature in the middle of the lithosphere (Figure 8), several other candidates could be proposed. The origin of high-conductivity anomalies in the deep lithosphere has been debated for decades [73]. Candidates proposed to interpret such anomalies in the mantle include aqueous fluids [74,75], partial melting [1,76], graphite [60,77], sulfides [77], magnetite-bearing serpentinite [78] and water dissolved in nominally anhydrous minerals or at grain boundaries [28,29,40,51,79,80]. Except for the latter, all the candidates seem unlikely, as discussed in Section 4.3. Contrastingly, hydrous garnet could explain the anomaly.

The minimum pressure for garnet stability in pyroxene-rich rocks can be as low as 1.25 GPa [33]. As a consequence, the presence of pyroxene-rich rocks at depths around 40 km or greater seems to be a reasonable alternative explanation for the high-conductivity bodies in the lithospheric mantle of the Cocos plate. This correlation is not sufficient to conclude but motivates conductivity modeling

in order to estimate the required amount of garnet to explain such anomalies under LAB conditions. The results of electrical conductivity modeling are presented in Section 3.3.

3.3. Garnet Networks Well Explain the Anomaly Offshore Nicaragua

Electrical conductivity simulations are presented in Figure 7, equations are provided in Table 1 and parameters and associated references in Table 2. Calculations are performed considering mantle pyroxenites with hydration levels and water partitioning consistent with the literature [63,64]. According to plate cooling, the anomaly offshore Nicaragua is located at depths between 40 and 60 km, where temperature lies between 1000 and 1100 °C and pressure between 1.3 and 1.8 GPa (Sections 1 and 3.1; Figure 8). Considering either dry MORB, pyroxenite or peridotite composition, these conditions are not compatible with partial melting (Figure 3a). Studies considering scenarios with reasonable hydration of peridotite provide results all incompatible with partial melting in such conditions (Figure 3b).

As seen in Figure 7, garnet composition and water content are key parameters controlling the ability of garnet to explain the observed conductivity values. Neither water alone (Figure 7a,c) nor the iron content alone (Figure 7b,d) suffices to reproduce the observations. Nonetheless, the combined effect of cations diversity and water is able to reproduce the observations either at 1000 °C (Figure 7b) or 1100 °C (Figure 7d). Considering 465 ppm H_2O in garnet, either the Hashin–Shtrikman upper bound or the modified brick-layer model shows that the garnet fraction required to reproduce the observations is 25–30 vol.%. Considering 160 ppm H_2O in garnet, the predicted garnet fraction would be 80–100 vol.% (Figure 7b,d).

A melt/glass/rock of MORB composition that enters the garnet stability field is expected to contain ≈18 wt.% of garnet after equilibration [24], and garnet websterites are generally assumed to contain ≈20% garnet [25]. As a consequence, assuming that (1) the anomaly originates from the presence of garnet pyroxenites and (2) the simplified mantle pyroxenites used in the model are representative of the conductive channels, the water content of the garnet should be relatively high (e.g., 465 ppm) as well as the iron content or cation diversity.

Using a modified Archie's law [54], the required garnet content drops to 20–25 vol.% ($1 < m < 1.2$; Figure 7). The m parameter of Archie's law contains implicit factors, such as the tortuosity of the conductive network. Increasing m in the model decreases the predicted garnet content of the pyroxenite. Importantly, it should be noted that the hydration level of ≈400 ppm required for the garnet to be conductive enough to explain MT data according to these models is comparable to water contents assumed in simulations of partial melting at P-T conditions relevant for the LAB.

The persistent anisotropic high-conductivity anomaly cannot be explained by the presence of melt, and it rather correlates with the stability of garnet in pyroxene-rich rocks. The latter likely emplace at the base of the early-stage lithosphere at relatively active spreading centers (see discussion in Section 4.1.2), and the formation of garnet within the latter is expected to occur with decreasing temperature as the plate gets older/colder (Figures 3 and 8), i.e., fossilized LAB (see discussion in Section 4.1.3). In contrast, as can be seen in Figure 3, it should be emphasized that garnet networks cannot explain the anomaly east of the EPR, where the presence of a melt network, as explained in the literature [1], is the most likely origin of high electrical conductivity values.

4. Discussion

Based on the results, I propose an integrated interpretation (Figures 8c and 9) of the synthetic electrical conductivity profile presented in Figure 8b. Here I discuss the origin of the deep pyroxenites (Section 4.1), the relevance of garnet as a realistic origin for high-conductivity values (Section 4.2) and the limitations of the model and remaining questions (Section 4.3).

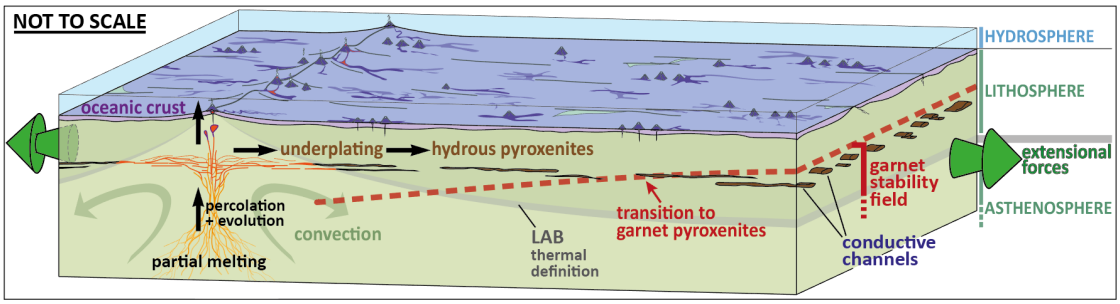

Figure 9. Simplified diagram highlighting the expected geometry of the fossilized channels. This model presents an interpretation slightly different from the one proposed in Figure 8c. Here the deep pyroxenites are subhorizontal from the moment of their formation and limited to a narrow depth window, which corresponds to the depth where interconnected melt has been detected. Contrastingly, in Figure 8c, off-axis shearing is proposed to impact the depth of the pyroxenite channels.

4.1. Origin of the Pyroxenite Channels

According to Section 3, hydrous garnet pyroxenites could explain the electrical anomaly offshore Nicaragua, contrary to partial melting, which is notably inconsistent with the plate cooling history.

4.1.1. Partial Melting and Melt Migration at the EPR

It is agreed that the formation of basaltic crust at ridges originates from the migration and accumulation of liquid silicates due to decompressional partial melting in adiabatic conditions at depths ranging from about 80 km to the base of the lithosphere ([81] and references therein). Extensive wetting of olivine grains forms interconnected intergranular networks [59] allowing melt transport in the hot mantle, starting at small melt fractions, rarely exceeding 2 vol.% [1–4,23,76,81]. Upward intergranular melt percolation and melt–rock interaction induce a dynamic source and a progressive evolution of its composition toward MORB [81,82].

Pyroxenites emplace by underplating at the base of the Ethiopian lithosphere [83], i.e., active rift, which could correspond to the initial stage of oceanization. In the eastern Pacific Ocean, a detailed study of a near-axis seamount chain revealed that seamounts are aligned parallel to the subaxial asthenospheric flow rather than absolute or relative plate motion vectors [70], which supports the underplating mechanism for pyroxenite emplacement into the oceanic LAB. In addition, LAB outcrops would be crosscut by a later generation of amphibole-bearing pyroxenite dykes [49], which suggest that melt emplacement can occur both at the ridge and, somewhat later, off axis. Melt would emplace off axis at depth during lithosphere formation at the ridge or result from the accumulation of a small degree of intraplate melting [16].

Lavas along the EPR axis consist of N-MORB with a homogenous composition whereas off-axis lavas have heterogeneous compositions, closer to E-MORB, which suggests that off-axis eruptions are fed by melt sills somehow disconnected from the axial magmatism [84]. In addition, geochemical data evidence that part of the partially molten triangle below ridges does not contribute to the formation of the oceanic crust but is trapped at depth [85].

4.1.2. Off-Axis Melt Percolation and Solidification

Considering shear strain at the LAB in the vicinity of the EPR, the conductive network can consist of either garnet grains connected to each other via shear-induced phase aggregation (e.g., [86]) or of a connected intergranular system corresponding to the fossilized network of melt trapped during underplating (inclusion of warm silicate liquid into colder rocks). Taking into account that, near the LAB, garnet is not stable in subsolidus conditions [30–34], garnet necessarily forms as a product of a metamorphic reaction at lower temperatures (<1200 °C) far from the ridge (Figure 8). The melt-trapping mechanism at the early-stage LAB could be creep cavitation pumping [87]. The conductive channels

could form through such a mechanism in the shear direction, which would be the deep equivalent of the observed off-axis lava transport [71]. The result of such a process would be the conductive melt channels hypothesized by previous studies [3,4,23], even though the fossilization of the channels into solid conductive features (Section 4.1.3) was not established.

The oceanic lithosphere does not necessarily include oceanic crust, and 25% of the oceanic floor likely consists of exhumed mantle rocks [88–91]. At a time, oceanic ridges can be characterized by the juxtaposition of both magma-rich and magma-poor segments [92,93], where coeval magmatism and mantle exhumation and serpentinization are reported [89,93]. The magma supply is not contiguous but rather consists of a discrete population of magma chambers aligned along the ridge. Studies showed that mantle diapirism along oceanic ridges can get fossilized within oceanic plates and that the spacing between these magma-rich zones is controlled by the overall activity of the spreading center and the asthenospheric flow [46,47,70].

As illustrated in Figures 2 and 9, non-hotspot seamounts are common features of the Pacific, Nazca and Cocos plates and are generally aligned in the spreading direction, e.g., [13,94]. This has been hypothesized to originate from small-scale convection that would occur normal to the plate-scale convection [13], but it could simply come from shear-induced melt segregation parallel to the main shear direction within the LAB [44,45,95]. Field studies investigating the nature of the LAB in the Oman ophiolite [46,47], as well as within the Lherz [49], Lanzo [48] and Ronda peridotites [96], report fossilized melt networks in the form of layered pyroxenites. Basaltic melt percolation in the Ronda peridotite is clearly identified by the presence of garnet pyroxenites [96].

The LAB can be seen as a thermal boundary layer at the base of which melt–rock reactions and magma ponding would weaken the lower lithosphere [97], which could favor its removal by mantle convection and feedback mechanisms involving further thermal/chemical erosion [96]. In the Ronda peridotite, a recrystallization front is highlighted, consisting of a sharp boundary between average mantle rocks and a domain characterized by an extensive percolation of basaltic melts [96].

4.1.3. LAB vs. Fossilized Early-Stage LAB

Partial melting at the LAB has been proposed as responsible for plate lubrication [98]. At the EPR, MT surveys show that the LAB reaches high electrical conductivity along the spreading direction (~8×10^{-2} S· m^{-1}) and significantly lower values parallel to the ridge (3×10^{-3} S·m^{-1}) [1,2]. Such conductivity values and contrasts could be explained by the presence of small amounts of melt aligned in the spreading direction [4,11,50]. In this case, because the conductivity of partially molten rocks is strongly dependent on the geometrical distribution of the melt [99], high melt connectivity is required [11]. Shear stress gradients [100] can trigger melt redistribution [7,95]. Hence, among the possible geometries and conductors, melt-rich channels recently became the only model able to account for observations of the LAB, e.g., [3,4]. However, other parameters are known to significantly increase the electrical conductivity, such as small grain size, which provides a high density of grain boundaries that transport charges [61,101], and the presence of volatiles that increase this GB diffusion [79].

By nature, the lower half of an oceanic lithosphere consists of the iterative stack of the fossilized base of younger oceanic lithospheres. As a consequence, a 23-Myr-old lithospheric mantle necessarily contains the fossilized trace of the early-stage lithosphere, which formed 23 million years earlier at an oceanic spreading ridge. As illustrated in Figure 8c, after shear-induced melt channelizing at the early-stage LAB near the EPR, the melt-bearing rocks would necessarily solidify, forming solid channels. At such a depth, the melt evolution is limited and should lead to an intermediate composition between pyroxenite and MORB. The melt network at grain boundaries is expected not to exceed ≈2% at a time (Section 4.1.1), but near-axis and off-axis melt pulses likely cumulate solidified melt networks iteratively, explaining the large volumes of pyroxenites usually identified on LAB outcrops [48,49,96].

MT has not revealed such a conductive layer in an older segment of the Pacific Plate (140–150 Ma) [102]. This could be interpreted as due to ridge asymmetry (Section 4.1.4) of the EPR system persistent over millions of years. However, the absence of an anomaly in older oceanic plates is rather

due to further plate cooling. The anomaly offshore Nicaragua is located at depths where temperatures are >1000 °C for a plate age of 20–25 Ma, consistent with the high conductivity of garnet pyroxenites (Section 3.3). The anomaly is expected to shut down in older plates (>45 Ma, i.e., <1000 °C at 60 km depth) [10].

4.1.4. Ridge Migration and Asymmetry

Asymmetry is a common feature of either slow- or fast-spreading centers [20]. The asymmetry of the EPR has been evidenced for many years [103–105]. A strong westward asymmetry is reported at the southern EPR and assumed to be the result of pressure or temperature gradients within the mantle [104,105]. The west subsides anomalously slowly compared to its equivalent in the Nazca plate [1], the latter being characterized by the high-conductivity anomaly (Figure 1a).

The ridge asymmetry is likely the consequence of its westward migration [104,105], although it seems not to suffice according to recent modeling [21]. The asymmetry along the southern EPR is likely the consequence of dynamic topography related to the superswell on the Pacific side [69].

Underplating may be discontinuous both in time and space as the accretion of pyroxene-rich cumulates at the early-stage LAB by iterative fossilization is more likely with increasing ridge lateral migration. Thus, for a given ridge segment, I suggest that the high-conductivity channels would preferentially exist in plate portions that formed in periods when the migration velocity was high compared to the average ridge velocity.

4.2. Garnet as a Viable Alternative to Melt in Electrical Models

Garnet, already proposed to explain high-conductivity anomalies in fossil subducted slabs [106] is conductive enough to explain the high-conductivity anomalies within the Cocos plate. Thanks to hydrogarnet substitution, garnet is able to bear significant amounts of water in mantle rocks (Section 4.2.1). In garnet pyroxenites, connected garnet networks could explain the observed electrical conductivity (Section 4.2.2).

Assuming a water content usually considered to explain partial melting in the mantle, i.e., 200–400 ppm (e.g., [30,107]), garnet may be conductive enough (Section 4.2.2), although additional components might help (Section 4.3). As highlighted in Section 2, such hydration levels are consistent with natural observations in mantle rocks collected either in Hawaii [64] or in South Africa [63]. Several other examples are listed in Section 4.2.2.

4.2.1. Widespread Hydrous Garnets in the Mantle

Although it is a nominally anhydrous mineral, garnet can contain significant amounts of H_2O either via hydrogarnet substitution (substitution of Si^{4+} by 4 H^+; Figure 4a) [108–110] or via a coupled substitution of Si^{4+} by [H^+ + Al^{3+}] [111]. The hydrogarnet defect is stabilized by hydrogen bonding (Figure 4a) [39]. Hydrogarnet is generally more stable in grossular ($Ca_3Al_2Si_3O_{12}$ = Grs_{100}), as documented by several studies [112–114]. However, it is demonstrably stable in pyrope ($Mg_3Al_2Si_3O_{12}$ = Py_{100}) in conditions relevant to the deep lithosphere (2.5 GPa, 1000 °C) [108]. Pyrope-rich garnets from the Colorado Plateau diatremes (Green Knobs, Garnet Ridge) reported by [109] contain up to 0.26 wt.% H_2O (2600 ppm). In the MgO-Al_2O_3-SiO_2 system, H_2O contents in synthetic pyrope are ≈0.05 wt.% (500 ppm) and consist of $(HO)_4^{4-}$ clusters. The H_2O content is ≈0.05 wt.% (500 ppm) in the Wesselton kimberlite (South Africa) and 0.09 wt.% (900 ppm) beneath the Udachnaya Craton [115]. In addition, the H_2O storage capacity of garnet is known to increase with Ti content [116].

The only studies that have investigated the electrical conductivity of hydrous garnets in conditions relevant for the deep lithosphere used pyrope from Garnet Ridge, Arizona, USA, of composition ~Py_{73}-Alm_{14}-Grs_{13} [28,29], with water contents of 465, 160 and 46 ppm. In addition, electrical conductivity measurements on peridotites and pyroxenites at 2–3 GPa (garnet stability field) in hydrous conditions (20–300 ppm water) reveal that pyroxenites are significantly more conductive [117],

unfortunately without microstructural imaging. The impact of the water content on the simulations is addressed in Figure 7.

4.2.2. Connectivity of Garnet Networks in Nature

Various natural rocks show garnet connectivity [26,118–121]. For example, garnet networks are documented in pyroxenite xenoliths from Southern Kenya (Figure 4a) [26], as well as in highly strained hydrous eclogite mylonites from the Norwegian Caledonides [119]. It is also reported, at least at the submeter scale, in an eclogite from the Zambian fossil subduction zone, where grain-boundary sliding induced phase aggregation and intergranular pressure solution connected the Fe-rich inner cores of the garnets [119]. Garnetite veins are also described in peridotites that endured metasomatism during the Caledonian orogeny [120]. They allow high garnet connectivity at the outcrop scale and the matrix of the metasomatized peridotites exhibits a poikilitic texture, which forms connected garnet networks in between the garnetite veins [120].

Mantle outcrops showing garnet connectivity [120] likely endured deformation and transformation during their exhumation. The only direct access to the deep lithospheric mantle is the study of xenoliths, e.g., [26,122,123]. Notably, mantle xenoliths document garnetite networks that grew at grain boundaries between large pyroxenes [26]. Such connected garnet networks originate from metamorphic reactions within the intergranular system, referred to as grain-boundary equilibrium [121]. I suggest that such garnet networks could form due to a metamorphic reaction between the pyroxene crystals and the melt percolating in between.

4.2.3. Destruction of the Conductive Channels at the Subduction Zone

The conductivity profile completely changes near the Nicaragua subduction (Figures 1b and 8). On the one hand, subduction consists of the sinking of a relatively cold lithosphere into the warm mantle, which necessarily decreases the temperature at a given depth (Figure 8b) and thus is expected to lower conductivity values by orders of magnitude, e.g., [28,101,124] (Figure 5). On the other hand, faults normal to the trench are needed at subduction zones to accommodate plate bending and bring water at depth [125–129], which should increase the electrical conductivity in the trench-parallel direction relative to the subduction direction, e.g., [130].

The spreading and subduction directions are not parallel (15° angle) and not exactly normal to the trench (Figure 2). Due to either plate bending or changes in shear directions, the fossilized channels, which are supposed to form at the young LAB due to shearing in the spreading direction [3,4], likely disorganize. As a consequence, the drastic drop of conductivity values at an ≈80 km depth at the subduction zone (Figure 8c) is likely due to the disorganization. Garnet networks would disconnect due to the damage of the pyroxenite channels.

4.3. Limitations and Remaining Questions

Usual candidates proposed to interpret such anomalies in the mantle include aqueous fluids (e.g., [74,75,131]), partial melting (e.g., [1,76]), graphite [60,77], sulfides [77] or magnetite-bearing serpentinite [78]. Tectonics, experimental petrology and geological observations provide complementary insights supporting the existence of pyroxenite channels in the fossilized LAB (Section 4.1). In addition, I show with thermodynamics considerations that anhydrous minerals containing ≈0.01–0.1 wt.% water constitute a viable candidate for explaining the electrical conductivity anomaly (Section 4.2).

4.3.1. Water Storage and Its Central Role

The hydration levels considered in the simulations (Section 3.3) are reasonable and consistent with natural observations [63,64]. They correspond to water contents typically considered to explain partial melting in the mantle, e.g., [30,107].

Olivine, the main component of the upper mantle, is not expected to melt at LAB P-T conditions, except in the presence of a high H_2O fraction [107]. Water, even in small amounts, lowers the melting

point of peridotite by ≈100 °C, which, for instance, induces partial melting in peridotite around 1300 °C considering San Carlos olivine and 0.32 wt.% (i.e., 3200 ppm) of H_2O [107], i.e., significant hydration, proposed by some studies to characterize the top of the asthenosphere, e.g., [50]. Considering high water contents locally within the pyroxenites, hydrous phases such as amphiboles could participate in the electrical circuit. For example, at 2–3 GPa, pargasite is stable up to 1075 °C [132].

Grain boundaries bear more water than the crystals themselves and constitute high-diffusivity pathways [61,101]. The structure of grain boundaries is still a matter of ongoing research [133,134], as well as the nature of interactions between water and crystals at grain boundaries [135,136]. Creep cavitation pumping has been evidenced as a deformation mechanism localizing both shear and melt/fluids [87,137–139]. A recent study explains the positive feedback between strain and water pumping in mantle shear zones [140]. Excess water due to strain localization [140] is not only due to smaller grain sizes and higher density of grain boundaries but by a significantly larger hydration level of the grain boundaries themselves in shear zones (1500–2000 ppm H_2O for initial bulk hydration of 1300 ppm) [140]. In Hawaii, where melt extraction is relatively efficient, garnet pyroxenite xenoliths are characterized by 260–576 ppm water [64].

Additional experiments and modeling are required to better understand the distribution of water defects in aggregates of nominally anhydrous minerals in order to get a better idea of conductive pathways either within conductive crystals or at grain boundaries. This question is not a matter of the current paper. As the connectivity problem, seen in terms of percolation, concerns both crystals and their boundaries, I argue that it is reasonable to consider that this question is not key to understanding the origin of the conductive anomaly at first order.

It is possible that the hydrous level of the fossilized melt channels is not as high as what the modeling (Figure 7) suggests, and it is likely that hydrous defects equivalent to intragranular hydrogarnet (Section 4.2.1) exist at grain boundaries. In other words, even though I consider in the present study a simple model with connected garnet crystals of constant electrical conductivity (for a given temperature), in nature, the conductivity likely varies from one crystal to another and between the core of crystals and their boundaries.

4.3.2. Garnet Stability vs. Small Grain Size

The electrical conductivity of natural pyroxenes and garnet with reasonable hydration are relatively similar (Figure 5), which brings back into question the causality between the presence of garnet networks and the higher conductivity values of the pyroxenite channels offshore Nicaragua. Upon conditions for garnet stability (≈1.8 GPa, 1100 °C, Figure 3a) are reached due to plate cooling, garnet grains should start nucleating at grain boundaries between pyroxene (± olivine) grains. Mineral transformations induce (transient) grain size reduction, which has important rheological implications [141–143]. Right after the entrance into the garnet stability field, grain-boundary equilibrium is expected [121].

This recalls that the electrical conductivity of mineral aggregates is controlled by both the nature of these minerals and the nature/structure of the grain boundaries, e.g., [101]. The entrance into the garnet stability field increases the density of grain boundaries, which necessarily increases the bulk conductivity. Whether or not the hydrogarnet defect is prominent in the fossilized LAB, the nucleation of garnet in between pyroxenes could significantly increase the bulk conductivity by increasing both the conductivity and connectivity of the high-conductivity pathways.

4.3.3. Additional Graphite

In the mantle, reduced conditions imply that carbon is more likely in the form of graphite that immobilizes at grain boundaries [144]. Conductive grain-boundary impurities significantly impact the bulk conductivity [60,77]. Graphite is very conductive over a wide temperature range (~10^5 S·m^{-1}) [145]. As a consequence, a small fraction suffices to significantly increase the conductivity if graphite impurities are connected throughout mantle peridotites [60]. However, a recent study revealed

that grain-boundary films are not stable and that graphite thus unlikely explains the high-conductivity anomalies revealed by MT surveys in the upper mantle [146].

The presence of small amounts of graphite within the fossilized LAB cannot be excluded. If some graphite (100 ppm or less) actually contributes to conductive networks in the oceanic mantle, the observed anomalies would require a slightly lower garnet fraction and/or connectivity.

4.3.4. Nature(s) of Lithosphere–Asthenosphere Boundaries

The anisotropic electrical anomaly offshore Nicaragua does not correspond to melt-bearing channels. This interpretation according to which horizontally extensive melt layers would persist and endure continuous shear over a confined depth of 40–60 km led to conclude that the anomaly was the LAB and, as a consequence, that the LAB consists of a population of thin, low-viscosity channels [3]. This definition of the LAB is in good agreement with geophysical observations, experimental petrology and thermodynamics considerations regarding very young oceanic plates (<5 Ma) [1], but it is demonstrably incorrect for older LABs (Section 3.1), where conductive anomalies are inexistent, limited or local (see the secondary anomaly at 90–110 km depth in Figures 1b and 8b). In Figure 8c, I interpret the secondary anomaly as due to melt percolation through the asthenosphere and local pooling at the top of the asthenosphere. This would be consistent with the suggested bending-induced partial melting [18].

Various definitions exist for the lithosphere, as detailed in the literature [147–149]. Each definition can be partially supported by some geophysical techniques (e.g., seismic, electrical and thermal definitions) or by speculations about the nature of the lithosphere (e.g., rheological, thermal and petrological definitions). Understanding the nature of the lithosphere, and thus the LAB, has been and will remain an interdisciplinary problem [149].

It seems relatively clear that the rheological lithosphere, i.e., the one useful for geodynamicists, tectonicists or seismologists, where decoupling may occur, is not associated with the same weakening mechanism everywhere on Earth. Although the young oceanic LAB would consist of a melt-rich layer, older LABs would rather be associated with premelting [150,151] or other transformations [42]. Each physical process would control the rheology of the LAB in a certain P-T window.

In all the above, I have discussed the structure of the present-day oceanic lithosphere and the nature of its lower limit. Nonetheless, the full understanding of the Earth's lithosphere also requires investigations of the nature and limits of the continental lithosphere [73,96,122,123,131,148,152], as well as the evolution of the lithosphere from the Early Earth [153–157] and the energy balance of mantle convection [158].

5. Conclusions

The electrical structure of the Cocos plate is reappraised into an integrated study in light of experimental results published over the past 20 years. The anisotropic conductive anomaly offshore Nicaragua is not the LAB and cannot be due to melt-bearing channels.

I propose a melt-free alternative model to explain the conductive channels offshore Nicaragua. I demonstrate that the presence of a fossilized early-stage LAB, in the form of garnet pyroxenites, can well explain the observed anomaly. Although the conductive channels do consist of melt-bearing rocks at the EPR, it fossilizes and progressively evolves into garnet pyroxenites with plate cooling.

For a reasonable water content consistent with natural observations, garnet pyroxenites should be considered among the candidates to explain such anomalies in light of the knowledge up to date. It is important to highlight that the hydration level that I consider in this study for the pyroxenite underplating is the one usually implemented in models that argue for partial melting in the uppermost asthenosphere. Here I show that melt-free interpretations are valid and that garnet pyroxenites are a good candidate to explain the anomaly offshore Nicaragua. Limited partial melting and pooling remain a reasonable explanation to account for the anomaly below the LAB, i.e., ≈40 km deeper than the main anomaly.

Additional surveys and experiments are needed to understand the nature of electrical anomalies in the lithosphere. As I highlight in this paper, these anomalies do not necessarily require the actual presence of melt, but partial melting of the mantle would remain a central process in the formation of the young LAB and its fossilization. Both the quantity and connectivity of garnet depend on the melt quantity and composition, and therefore on the activity of the ridges, known to vary both in time and space [85,93]. In addition, the anomaly is expected to shut down with increasing plate age (>45 Ma; Section 4.1.3), consistently with MT observations in the older oceanic lithosphere [102]. Consequently, the high-conductivity anomalies should not be expected to be systematically present in the oceanic lithosphere.

Furthermore, interrogations remain regarding the origin of conductive electrical anomalies in the continental lithosphere, e.g., North China Craton [159], Tanzanian Craton [160] or Mongolia [131]. The importance of garnet-rich rocks appears underestimated in interpretations of both the oceanic [1,3,4,23] and continental [123,131,159,160] lithospheres.

Funding: This research received no external funding.

Acknowledgments: I thank Rob Evans, Christian Chopin and Timm John for the key discussions, as well as two anonymous reviewers for constructive criticism. Additionally, I thank Pascale and Philippe Ferrand, my parents, for their support whenever peers or institutions have been a hindrance to my research.

Conflicts of Interest: The author declares no conflict of interest.

References

1. Evans, R.L.; Hirth, G.; Baba, K.; Forsyth, D.; Chave, A.; Mackie, R. Geophysical evidence from the MELT area for compositional controls on oceanic plates. *Nature* **2005**, *437*, 249–252. [CrossRef] [PubMed]
2. Baba, K.; Chave, A.D.; Evans, R.L.; Hirth, G.; Mackie, R.L. Mantle dynamics beneath the East Pacific Rise at 17 S: Insights from the Mantle Electromagnetic and Tomography (MELT) experiment. *J. Geophys. Res. Space Phys.* **2006**, *111*, B02101. [CrossRef]
3. Naif, S.; Key, K.; Constable, S.; Evans, R.L. Melt-rich channel observed at the lithosphere-asthenosphere boundary. *Nature* **2013**, *495*, 356. [CrossRef] [PubMed]
4. Caricchi, L.; Gaillard, F.; Mecklenburgh, J.; Le Trong, E. Experimental determination of electrical conductivity during deformation of melt-bearing olivine aggregates: Implications for electrical anisotropy in the oceanic low velocity zone. *Earth Planet. Sci. Lett.* **2011**, *302*, 81–94. [CrossRef]
5. Gaillard, F. Laboratory measurements of electrical conductivity of hydrous and dry silicic melts under pressure. *Earth Planet. Sci. Lett.* **2004**, *218*, 215–228. [CrossRef]
6. Anderson, D.L. The thermal state of the upper mantle; no role for mantle plumes. *Geophys. Res. Lett.* **2000**, *27*, 3623–3626. [CrossRef]
7. Takei, Y.; Holtzman, B.K. Viscous constitutive relations of solid-liquid composites in terms of grain boundary contiguity: 1. Grain boundary diffusion control model. *J. Geophys. Res. Space Phys.* **2009**, *114*, B06205. [CrossRef]
8. Sakamaki, T.; Suzuki, A.; Ohtani, E.; Terasaki, H.; Urakawa, S.; Katayama, Y.; Funakoshi, K.-I.; Wang, Y.; Hernlund, J.W.; Ballmer, M.D. Ponded melt at the boundary between the lithosphere and asthenosphere. *Nat. Geosci.* **2013**, *6*, 1041–1044. [CrossRef]
9. Lewis, B.T. The East Pacific Rise and the thermal model. *J. Geophys. Res. Space Phys.* **1983**, *88*, 3348. [CrossRef]
10. Ritzwoller, M.H.; Shapiro, N.M.; Zhong, S. Cooling history of the Pacific lithosphere. *Earth Planet. Sci. Lett.* **2004**, *226*, 69–84. [CrossRef]
11. Gaillard, F.; Malki, M.; Iacono-Marziano, G.; Pichavant, M.; Scaillet, B. Carbonatite melts and electrical conductivity in the asthenosphere. *Science* **2008**, *322*, 1363–1365. [CrossRef] [PubMed]
12. Zhu, W.; Gaetani, G.A.; Fusseis, F.; Montési, L.G.J.; De Carlo, F. Microtomography of partially molten rocks: Three-dimensional melt distribution in mantle peridotite. *Science* **2011**, *332*, 88–91. [CrossRef] [PubMed]
13. Ballmer, M.D.; van Hunen, J.; Ito, G.; Tackley, P.J.; Bianco, T.A. Non-hotspot volcano chains originating from small-scale sublithospheric convection. *Geophys. Res. Lett.* **2007**, *34*, L23310. [CrossRef]
14. Katz, R.F. Magma dynamics with the enthalpy method: Benchmark solutions and magmatic focusing at mid-ocean ridges. *J. Pet.* **2008**, *49*, 2099–2121. [CrossRef]

15. Höink, T.; Jellinek, A.M.; Lenardic, A. Viscous coupling at the lithosphere-asthenosphere boundary. *Geochem. Geophys. Geosystems* **2011**, *12*. [CrossRef]
16. Hirschmann, M.M. Partial melt in the oceanic low velocity zone. *Phys. Earth Planet. Inter.* **2010**, *179*, 60–71. [CrossRef]
17. Kohlstedt, D.L.; Holtzman, B.K. Shearing melt out of the Earth: An experimentalist's perspective on the influence of deformation on melt extraction. *Annu. Rev. Earth Planet Sci.* **2009**, *37*, 561–593. [CrossRef]
18. Evans, R.L.; Sarafian, E.; Sarafian, A.R. The Evolution of the Oceanic Lithosphere: An Electromagnetic Perspective. In *Lithospheric Discontinuities*; Wiley: Hoboken, NJ, USA, 2018; pp. 35–53.
19. Commission for the Geological Map of the World; Bouysse, P.; Acharyya, S.K.; Bischoff, D. *Geological Map of the World at 1:35 000 000*, 3rd ed.; CCGM-CGMW: Paris, France, 2014; ISBN 978-2-917310-24-3.
20. Müller, R.D.; Sdrolias, M.; Gaina, C.; Roest, W.R. Age, spreading rates, and spreading asymmetry of the world's ocean crust. *Geochem. Geophys. Geosyst.* **2008**, *9*. [CrossRef]
21. Key, K.; Constable, S.; Liu, L.; Pommier, A. Electrical image of passive mantle upwelling beneath the northern East Pacific Rise. *Nature* **2013**, *495*, 499–502. [CrossRef] [PubMed]
22. Lonsdale, P. Structural geomorphology of a fast-spreading rise crest: The East Pacific Rise near 3°25′ S. *Mar. Geophys. Res.* **1977**, *3*, 251–293. [CrossRef]
23. Laumonier, M.; Farla, R.; Frost, D.J.; Katsura, T.; Marquardt, K.; Bouvier, A.S.; Baumgartner, L.P. Experimental determination of melt interconnectivity and electrical conductivity in the upper mantle. *Earth Planet. Sci. Lett.* **2017**, *463*, 286–297. [CrossRef]
24. Pertermann, M.; Hirschmann, M.M. Anhydrous partial melting experiments on MORB-like eclogite: Phase relations, phase compositions and mineral-melt partitioning of major elements at 2–3 GPa. *J. Petrol.* **2003**, *44*, 2173–2201. [CrossRef]
25. Hirschmann, M.M.; Stolper, E.M. A possible role for garnet pyroxenite in the origin of the "garnet signature" in MORB. *Contrib. Miner. Petrol.* **1996**, *124*, 185–208. [CrossRef]
26. Henjes-Kunst, F.; Altherr, R. Metamorphic petrology of xenoliths from Kenya and northern Tanzania and implications for geotherms and lithospheric structures. *J. Petrol.* **1992**, *33*, 1125–1156. [CrossRef]
27. Romano, C.; Poe, B.T.; Kreidie, N.; McCammon, C.A. Electrical conductivities of pyrope-almandine garnets up to 19 GPa and 1700 °C. *Am. Mineral.* **2006**, *91*, 1371–1377. [CrossRef]
28. Dai, L.; Li, H.; Hu, H.; Shan, S.; Jiang, J.; Hui, K. The effect of chemical composition and oxygen fugacity on the electrical conductivity of dry and hydrous garnet at high temperatures and pressures. *Contrib. Mineral. Petrol.* **2012**, *163*, 689–700. [CrossRef]
29. Dai, L.; Karato, S.I. Electrical conductivity of pyrope-rich garnet at high temperature and high pressure. *Phys. Earth Planet Inter.* **2009**, *176*, 83–88. [CrossRef]
30. Hirschmann, M.M.; Tenner, T.; Aubaud, C.; Withers, A.C. Dehydration melting of nominally anhydrous mantle: The primacy of partitioning. *Phys. Earth Planet Inter.* **2009**, *176*, 54–68. [CrossRef]
31. Gudfinnsson, G.H.; Presnall, D.C. Melting relations of model lherzolite in the system CaO-MgO-Al_2O_3-SiO_2 at 2.4–3.4 GPa and the generation of komatiites. *J. Geophys. Res. Solid Earth* **1996**, *101*, 27701–27709. [CrossRef]
32. Green, D.H.; Ringwood, A.E. A comparison of recent experimental data on the gabbro-garnet granulite-eclogite transition. *J. Geol.* **1972**, *80*, 277–288. [CrossRef]
33. Irving, A.J. Geochemical and high-pressure experimental studies of garnet pyroxenite and pyroxene granulite xenoliths from the Delegate basaltic pipes, Australia. *J. Petrol.* **1974**, *15*, 1–40. [CrossRef]
34. Kogiso, T.; Hirschmann, M.M.; Frost, D.J. High-pressure partial melting of garnet pyroxenite: Possible mafic lithologies in the source of ocean island basalts. *Earth Planet Sci. Lett.* **2003**, *216*, 603–617. [CrossRef]
35. O'Hara, M.J.; Richardson, S.W.; Wilson, G. Garnet-peridotite stability and occurrence in crust and mantle. *Contrib. Miner. Petrol.* **1971**, *32*, 48–68. [CrossRef]
36. Sarafian, E.; Gaetani, G.A.; Hauri, E.H.; Sarafian, A.R. Experimental constraints on the damp peridotite solidus and oceanic mantle potential temperature. *Science* **2017**, *355*, 942–945. [CrossRef] [PubMed]
37. Novak, G.A.; Gibbs, G.V. The crystal chemistry of the silicate garnets. *Am. Miner.* **1971**, *56*, 791–825.
38. Wright, K.; Freer, R.; Catlow, C.R.A. The energetics and structure of the hydrogarnet defect in grossular: A computer simulation study. *Phys. Chem. Miner.* **1974**, *20*, 500–503. [CrossRef]
39. Lacivita, V.; Mahmoud, A.; Erba, A.; D'Arco, P.; Mustapha, S. Hydrogrossular, $Ca_3Al_2(SiO_4)_{3-x}(H_4O_4)_x$: An ab initio investigation of its structural and energetic properties. *Am. Mineral.* **2015**, *100*, 2637–2649. [CrossRef]

40. Dai, L.; Karato, S.I. Electrical conductivity of orthopyroxene: Implications for the water content of the asthenosphere. *Proc. Jpn. Acad. Ser. B* **2009**, *85*, 466–475. [CrossRef]
41. Hirschmann, M.M. The mantle solidus: Experimental constraints and the effects of peridotite composition. *Geochem. Geophys. Geosystems* **2000**, *1*, 10. [CrossRef]
42. Ferrand, T.P.; Koizumi, S.; Deldicque, D. Unexpected softening of Mg_2GeO_4 with minor $MgGeO_3$ between 1000 and 1150 °C. Unpublished work, 2020.
43. Schmeling, H. Numerical models on the influence of partial melt on elastic, anelastic and electrical properties of rocks. Part II: Electrical conductivity. *Phys. Earth Planet Inter.* **1986**, *43*, 123–136. [CrossRef]
44. Rabinowicz, M.; Toplis, M.J. Melt segregation in the lower part of the partially molten mantle zone beneath an oceanic spreading centre: Numerical modelling of the combined effects of shear segregation and compaction. *J. Petrol.* **2009**, *50*, 1071–1106. [CrossRef]
45. Rabinowicz, M.; Vigneresse, J.L. Melt segregation under compaction and shear channeling: Application to granitic magma segregation in a continental crust. *J. Geophys. Res. Solid Earth* **2004**, *109*. [CrossRef]
46. Nicolas, A.; Ceuleneer, G.; Boudier, F.; Misseri, M. Structural mapping in the Oman ophiolites: Mantle diapirism along an oceanic ridge. *Tectonophysics* **1988**, *151*, 27–56. [CrossRef]
47. Ceuleneer, G.; Nicolas, A.; Boudier, F. Mantle flow patterns at an oceanic spreading centre: The Oman peridotites record. *Tectonophysics* **1988**, *151*, 1–26. [CrossRef]
48. Lorand, J.P.; Keays, R.R.; Bodinier, J.L. Copper and noble metal enrichments across the lithosphere-asthenosphere boundary of mantle diapirs: Evidence from the Lanzo lherzolite massif. *J. Petrol.* **1993**, *34*, 1111–1140. [CrossRef]
49. Le Roux, V.; Tommasi, A.; Vauchez, A. Feedback between melt percolation and deformation in an exhumed lithosphere-asthenosphere boundary. *Earth Planet Sci. Lett.* **2008**, *274*, 401–413. [CrossRef]
50. Yoshino, T.; Matsuzaki, T.; Yamashita, S.; Katsura, T. Hydrous olivine unable to account for conductivity anomaly at the top of the asthenosphere. *Nature* **2006**, *443*, 973–976. [CrossRef]
51. Gardés, E.; Gaillard, F.; Tarits, P. Toward a unified hydrous olivine electrical conductivity law. *Geochem. Geophys. Geosyst.* **2014**, *15*, 4984–5000. [CrossRef]
52. Yang, X.; Keppler, H.; McCammon, C.; Ni, H.; Xia, Q.; Fan, Q. Effect of water on the electrical conductivity of lower crustal clinopyroxene. *J. Geophys. Res. Solid Earth* **2011**, *116*, B4. [CrossRef]
53. Riley, G.N., Jr.; Kohlstedt, D.L.; Richter, P.M. Melt migration in a silicate liquid-olivine system: An experimental test of compaction theory. *Geophys. Res. Lett.* **1990**, *17*, 2101–2104. [CrossRef]
54. Glover, P.W.; Hole, M.J.; Pous, J. A modified Archie's law for two conducting phases. *Earth Planet Sci. Lett.* **2000**, *180*, 369–383. [CrossRef]
55. Hashin, Z.; Shtrikman, S. A variational approach to the theory of the effective magnetic permeability of multiphase materials. *J. Appl. Phys.* **1962**, *33*, 3125–3131. [CrossRef]
56. Grant, F.S.; West, G.F. *Interpretation Theory in Applied Geophysics*; McGraw-Hill Book: New York, USA, 1965.
57. Waff, H.S. Theoretical considerations of electrical conductivity in a partially molten mantle and implications for geothermometry. *J. Geophys. Res.* **1974**, *79*, 4003–4010. [CrossRef]
58. Partzsch, G.M. Elektrische Leitfähigkeit Partiell Geschmolzener Gesteine: Experimentelle Untersuchungen, Modellrechnungen und Interpretation Einer Elektrisch Leitfähigken Zone in den Zentralen Anden. Ph.D. Thesis, Freie Universität, Berlin, Germany, 1997.
59. Miller, K.J.; Montési, L.G.; Zhu, W.L. Estimates of olivine-basaltic melt electrical conductivity using a digital rock physics approach. *Earth Planet Sci. Lett.* **2015**, *432*, 332–341. [CrossRef]
60. Wang, D.; Karato, S.I.; Jiang, Z. An experimental study of the influence of graphite on the electrical conductivity of olivine aggregates. *Geophys. Res. Lett.* **2013**, *40*, 2028–2032. [CrossRef]
61. Ten Grotenhuis, S.M.; Drury, M.R.; Peach, C.J.; Spiers, C.J. Electrical properties of fine-grained olivine: Evidence for grain boundary transport. *J. Geophys. Res. Solid Earth* **2004**, *109*, B0623. [CrossRef]
62. Stauffer, D.; Aharony, A. *Introduction to Percolation Theory*, 2nd ed.; Taylor, Francis: Abingdon, UK, 1992.
63. Beran, A.; Libowitzky, E. Water in natural mantle minerals II: Olivine, garnet and accessory minerals. *Rev. Mineral. Geochem.* **2006**, *62*, 169–191. [CrossRef]
64. Bizimis, M.; Peslier, A.H. Water in Hawaiian garnet pyroxenites: Implications for water heterogeneity in the mantle. *Chem. Geol.* **2015**, *397*, 61–75. [CrossRef]

65. Archie, G.E. The electrical resistivity log as an aid in determining some reservoir characteristics. *Trans. AIME* **1942**, *146*, 54–62. [CrossRef]
66. Klemme, S.; O'Neill, H.S. The near-solidus transition from garnet lherzolite to spinel lherzolite. *Contrib. Mineral. Petrol.* **2000**, *138*, 237–248. [CrossRef]
67. Bown, J.W.; White, R.S. Variation with spreading rate of oceanic crustal thickness and geochemistry. *Earth Planet Sci. Lett.* **1994**, *121*, 435–449. [CrossRef]
68. Bonini, M. Seismic loading of fault-controlled fluid seepage systems by great subduction earthquakes. *Sci. Rep.* **2009**, *9*, 1–12. [CrossRef] [PubMed]
69. Steinberger, B. Topography caused by mantle density variations: Observation-based estimates and models derived from tomography and lithosphere thickness. *Geophys. Suppl. Mon. Not. R. Astron. Soc.* **2016**, *205*, 604–621. [CrossRef]
70. Clague, D.A.; Reynolds, J.R.; Davis, A.S. Near-ridge seamount chains in the northeastern Pacific Ocean. *J. Geophys. Res. Solid Earth* **2000**, *105*, 16541–16561. [CrossRef]
71. Soule, S.A.; Fornari, D.J.; Perfit, M.R.; Tivey, M.A.; Ridley, W.I.; Schouten, H. Channelized lava flows at the East Pacific Rise crest 9–10 N: The importance of off-axis lava transport in developing the architecture of young oceanic crust. *Geochem. Geophys. Geosyst.* **2005**, *6*. [CrossRef]
72. Yasuda, A.; Fujii, T.; Kurita, K. Melting phase relations of an anhydrous mid-ocean ridge basalt from 3 to 20 GPa: Implications for the behavior of subducted oceanic crust in the mantle. *J. Geophys. Res. Solid Earth* **1994**, *99*, 9401–9414. [CrossRef]
73. Jones, A.G. Imaging the continental upper mantle using electromagnetic methods. *Dev. Geotecton.* **1999**, *24*, 57–80.
74. Shimojuku, A.; Yoshino, T.; Yamazaki, D.; Okudaira, T. Electrical conductivity of fluid-bearing quartzite under lower crustal conditions. *Phys. Earth Planet Inter.* **2012**, *198*, 1–8. [CrossRef]
75. Shimojuku, A.; Yoshino, T.; Yamazaki, D. Electrical conductivity of brine-bearing quartzite at 1 GPa: Implications for fluid content and salinity of the crust. *Earth Planets Space* **2014**, *66*, 2. [CrossRef]
76. Shankland, T.J.; Waff, H.S. Partial melting and electrical conductivity anomalies in the upper mantle. *J. Geophys. Res.* **1977**, *82*, 5409–5417. [CrossRef]
77. Watson, H.C.; Roberts, J.J.; Tyburczy, J.A. Effect of conductive impurities on electrical conductivity in polycrystalline olivine. *Geophys. Res. Lett.* **2010**, *37*, L02302. [CrossRef]
78. Kawano, S.; Yoshino, T.; Katayama, I. Electrical conductivity of magnetite-bearing serpentinite during shear deformation. *Geophys. Res. Lett.* **2012**, *39*, L20313. [CrossRef]
79. Karato, S. The role of hydrogen in the electrical conductivity of the upper mantle. *Nature* **1990**, *347*, 272–273. [CrossRef]
80. Wang, D.; Mookherjee, M.; Xu, Y.; Karato, S. The effect of water on the electrical conductivity of olivine. *Nature* **2006**, *443*, 977–980. [CrossRef] [PubMed]
81. Langmuir, C.H.; Klein, E.M.; Plank, T. Petrological systematics of mid-ocean ridge basalts: Constraints on melt generation beneath ocean ridges. *Mantle Flow Melt Gener. Mid Ocean Ridges* **1992**, *71*, 183–280.
82. Kamenetsky, V.S.; Maas, R. Mantle-melt evolution (dynamic source) in the origin of a single MORB suite: A perspective from magnesian glasses of Macquarie Island. *J. Petrol.* **2002**, *43*, 1909–1922. [CrossRef]
83. Rooney, T.O.; Lavigne, A.; Svoboda, C.; Girard, G.; Yirgu, G.; Ayalew, D.; Kappelman, J. The making of an underplate: Pyroxenites from the Ethiopian lithosphere. *Chem. Geol.* **2017**, *455*, 264–281. [CrossRef]
84. Vithana, M.V.P.; Xu, M.; Zhao, X.; Zhang, M.; Luo, Y. Geological and geophysical signatures of the East Pacific Rise 8°–10° N. *Solid Earth Sci.* **2019**, *4*, 66–83. [CrossRef]
85. Wanless, V.D.; Behn, M.D. Spreading rate-dependent variations in crystallization along the global mid-ocean ridge system. *Geochem. Geophys. Geosyst.* **2017**, *18*, 3016–3033. [CrossRef]
86. Hiraga, T.; Miyazaki, T.; Yoshida, H.; Zimmerman, M.E. Comparison of microstructures in superplastically deformed synthetic materials and natural mylonites: Mineral aggregation via grain boundary sliding. *Geology* **2013**, *41*, 959–962. [CrossRef]
87. Fusseis, F.; Regenauer-Lieb, K.; Liu, J.; Hough, R.M.; De Carlo, F. Creep cavitation can establish a dynamic granular fluid pump in ductile shear zones. *Nature* **2009**, *459*, 974–977. [CrossRef] [PubMed]
88. Cannat, M.; Sauter, D.; Lavier, L.; Bickert, M.; Momoh, E.; Leroy, S. On spreading modes and magma supply at slow and ultraslow mid-ocean ridges. *Earth Planet. Sci. Lett.* **2019**, *519*, 223–2330. [CrossRef]

89. Cannat, M.; Fontaine, F.; Escartin, J. Serpentinization and associated hydrogen and methane fluxes at slow spreading ridges. In *Diversity of Hydrothermal Systems on Slow Spreading Ocean Ridges 188*; AGU: Washington, DC, USA, 2010; pp. 241–264.
90. Bickert, M.; Lavier, L.; Cannat, M. How do detachment faults form at ultraslow mid-ocean ridges in a thick axial lithosphere? *Earth Planet Sci. Lett.* **2020**, *533*, 116048. [CrossRef]
91. Ferrand, T.P. Transition from amagmatic to volcanic margin: Mantle exhumation in the Vøring Basin before the Icelandic plume influence. *Tectonophysics* **2020**, *776*, 228319. [CrossRef]
92. Cannat, M.; Sauter, D.; Mendel, V.; Ruellan, E.; Okino, K.; Escartin, J.; Combier, V.; Baala, M. Modes of seafloor generation at a melt-poor ultraslow-spreading ridge. *Geology* **2006**, *34*, 605–608. [CrossRef]
93. Paquet, M.; Cannat, M.; Brunelli, D.; Hamelin, C.; Humler, E. Effect of melt/mantle interactions on MORB chemistry at the easternmost Southwest Indian Ridge (61°–67° E). *Geochem. Geophys. Geosyst.* **2016**, *17*, 4605–4640. [CrossRef]
94. Fornari, D.J.; Ryan, W.B.; Fox, P.J. Sea-floor lava fields on the East Pacific Rise. *Geology* **1985**, *13*, 413–416. [CrossRef]
95. Holtzman, B.K.; Groebner, N.J.; Zimmerman, M.E.; Ginsberg, S.B.; Kohlstedt, D.L. Stress-driven melt segregation in partially molten rocks. *Geochem. Geophys. Geosyst.* **2003**, *4*, 5. [CrossRef]
96. Lenoir, X.; Garrido, C.J.; Bodinier, J.L.; Dautria, J.M.; Gervilla, F. The recrystallization front of the Ronda peridotite: Evidence for melting and thermal erosion of subcontinental lithospheric mantle beneath the Alboran Basin. *J. Petrol.* **2001**, *42*, 141–158. [CrossRef]
97. Xu, Y.G.; Menzies, M.A.; Bodinier, J.L.; Bedini, R.M.; Vroon, P.; Mercier, J.C. Melt percolation and reaction atop a plume: Evidence from the poikiloblastic peridotite xenoliths from Borée (Massif Central, France). *Contrib. Mineral. Petrol.* **1998**, *132*, 65–84. [CrossRef]
98. Holtzman, B.K.; Kendall, J.M. Organized melt, seismic anisotropy, and plate boundary lubrication. *Geochem. Geophys. Geosyst.* **2010**, *11*, 12. [CrossRef]
99. Roberts, J.J.; Tyburczy, J.A. Partial-melt electrical conductivity: Influence of melt composition. *J. Geophys. Res. Solid Earth* **1999**, *104*, 7055–7065. [CrossRef]
100. Turcotte, D.L.; Schubert, G. *Geodynamics*; Cambridge University Press: Cambridge, UK, 2002.
101. Pommier, A.; Kohlstedt, D.L.; Hansen, L.N.; Mackwell, S.; Tasaka, M.; Heidelbach, F.; Leinenweber, K. Transport properties of olivine grain boundaries from electrical conductivity experiments. *Contrib. Mineral. Petrol.* **2018**, *173*, 41. [CrossRef]
102. Matsuno, T.; Seama, N.; Evans, R.; Chave, A.D.; Baba, K.; White, A.; Goto, T.-N.; Heinson, G.; Boren, G.; Yoneda, A.; et al. Upper mantle electrical resistivity structure beneath the central Mariana subduction system. *Geochem. Geophys. Geosyst.* **2010**, *11*, 9. [CrossRef]
103. Evans, R.L.; Tarits, P.; Chave, A.D.; White, A.; Heinson, G.; Filloux, J.H.; Toh, H.; Seama, N.; Utada, H.; Booker, J.R.; et al. Asymmetric electrical structure in the mantle beneath the East Pacific Rise at 17° S. *Science* **1999**, *286*, 752–756. [CrossRef]
104. Conder, J.A.; Forsyth, D.W.; Parmentier, E.M. Asthenospheric flow and asymmetry of the East Pacific Rise, MELT area. *J. Geophys. Res.* **2002**, *107*, 2344. [CrossRef]
105. Toomey, D.R.; Wilcock, W.S.D.; Conder, J.A.; Forsyth, D.W.; Blundy, J.D.; Parmentier, E.M.; Hammond, W.C. Asymmetric mantle dynamics in the MELT region of the East Pacific Rise. *Earth Planet Sci. Lett.* **2002**, *200*, 287–295. [CrossRef]
106. Evans, R.; Jones, A.G.; Garcia, X.; Muller, M.; Hamilton, M.; Evans, S.; Fourie, C.J.S.; Spratt, J.; Webb, S.; Jelsma, H.; et al. Electrical lithosphere beneath the Kaapvaal craton, southern Africa. *J. Geophys. Res. Solid Earth* **2011**, *116*, B4. [CrossRef]
107. Gaetani, G.A.; Grove, T.L. The influence of water on melting of mantle peridotite. *Contrib. Mineral. Petrol.* **1998**, *131*, 323–346. [CrossRef]
108. Ackermann, L.; Cemič, L.; Langer, K. Hydrogarnet substitution in pyrope: A possible location for "water" in the mantle. *Earth Planet Sci. Lett.* **1983**, *62*, 208–214. [CrossRef]
109. Aines, R.D.; Rossman, G.R. Water content of mantle garnets. *Geology* **1984**, *12*, 720–723. [CrossRef]
110. Katayama, I.; Hirose, K.; Yurimoto, H.; Nakashima, S. Water solubility in majoritic garnet in subducting oceanic crust. *Geophys. Res. Lett.* **2003**, *30*, 22. [CrossRef]
111. Mookherjee, M.; Karato, S.I. Solubility of water in pyrope-rich garnet at high pressures and temperature. *Geophys. Res. Lett.* **2010**, *37*, 3. [CrossRef]

112. Withers, A.C.; Wood, B.J.; Carroll, M.R. The OH content of pyrope at high pressure. *Chem. Geol.* **1998**, *147*, 161–171. [CrossRef]
113. Geiger, C.A.; Rossman, G.R. Micro- and nano-size hydrogarnet clusters and proton ordering in calcium silicate garnet: Part I. The quest to understand the nature of "water" in garnet continues. *Am. Miner.* **2020**, *105*, 455–467. [CrossRef]
114. Geiger, C.A.; Rossman, G.R. IR spectroscopy and OH^- in silicate garnet: The long quest to document the hydrogarnet substitution. *Am. Miner.* **2018**, *103*, 384–393. [CrossRef]
115. Maldener, J.; Hösch, A.; Langer, K.; Rauch, F. Hydrogen in some natural garnets studied by nuclear reaction analysis and vibrational spectroscopy. *Phys. Chem. Miner.* **2003**, *30*, 337–344. [CrossRef]
116. Reynes, J.; Lanari, P.; Hermann, J. A mapping approach for the investigation of Ti–OH relationships in metamorphic garnet. *Contrib. Miner. Pet.* **2020**, *175*, 1–17. [CrossRef]
117. Wang, D.; Li, H.; Yi, L.; Shi, B. The electrical conductivity of upper-mantle rocks: Water content in the upper mantle. *Phys. Chem. Miner.* **2007**, *35*, 157–162. [CrossRef]
118. John, T.; Scherer, E.; Haase, K.; Schenk, V. Trace element fractionation during fluid-induced eclogitization in a subducting slab: Trace element and Lu–Hf–Sm–Nd isotope systematics. *Earth Planet. Sci. Lett.* **2004**, *227*, 441–456. [CrossRef]
119. Smit, M.A.; Scherer, E.E.; John, T.; Janssen, A. Creep of garnet in eclogite: Mechanisms and implications. *Earth Planet. Sci. Lett.* **2011**, *311*, 411–419. [CrossRef]
120. Vrijmoed, J.C.; Austrheim, H.; John, T.; Hin, R.C.; Corfu, F.; Davies, G.R. Metasomatism in the ultrahigh-pressure Svartberget garnet-peridotite (Western Gneiss Region, Norway): Implications for the transport of crust-derived fluids within the mantle. *J. Pet.* **2013**, *54*, 1815–1848. [CrossRef]
121. Lanari, P.; Engi, M. Local bulk composition effects on metamorphic mineral assemblages. *Rev. Miner. Geochem.* **2017**, *83*, 55–102. [CrossRef]
122. Chin, E.J. Deep crustal cumulates reflect patterns of continental rift volcanism beneath Tanzania. *Contrib. Miner. Pet.* **2018**, *173*, 85. [CrossRef]
123. Ferrand, T.P. Garnet pyroxenites explain high electrical conductivity in the East African deep lithosphere. *Nature*. submitted.
124. Karato, S.-I.; Wang, D. Electrical Conductivity of Minerals and Rocks. *Phys. Chem. Deep Earth* **2013**, *5*, 145–182.
125. Ranero, C.R.; Morgan, J.P.; McIntosh, K.; Reichert, C. Bending-related faulting and mantle serpentinization at the Middle America trench. *Nat. Cell Biol.* **2003**, *425*, 367–373. [CrossRef]
126. Kita, S.; Ferrand, T.P. Physical mechanisms of oceanic mantle earthquakes: Comparison of natural and experimental events. *Sci. Rep.* **2018**, *8*, 17049. [CrossRef] [PubMed]
127. Cai, C.; Wiens, D.A.; Shen, W.; Eimer, M. Water input into the Mariana subduction zone estimated from ocean-bottom seismic data. *Nat. Cell Biol.* **2018**, *563*, 389–392. [CrossRef]
128. Ferrand, T.P. Seismicity and mineral destabilizations in the subducting mantle up to 6 GPa, 200 km depth. *Lithos* **2019**, *334*, 205–230. [CrossRef]
129. Boneh, Y.; Schottenfels, E.; Kwong, K.; van Zelst, I.; Tong, X.; Eimer, M.; Miller, M.S.; Moresi, L.; Warren, J.M.; Wiens, D.A.; et al. Intermediate-Depth Earthquakes Controlled by Incoming Plate Hydration Along Bending-Related Faults. *Geophys. Res. Lett.* **2019**, *46*, 3688–3697. [CrossRef]
130. Wang, D.; Guo, Y.; Yu, Y.; Karato, S.-I. Electrical conductivity of amphibole-bearing rocks: Influence of dehydration. *Contrib. Miner. Pet.* **2012**, *164*, 17–25. [CrossRef]
131. Comeau, M.J.; Becken, M.; Connolly, J.A.D.; Grayver, A.V.; Kuvshinov, A.V. Compaction-Driven Fluid Localization as an Explanation for Lower Crustal Electrical Conductors in an Intracontinental Setting. *Geophys. Res. Lett.* **2020**, *47*, e2020GL088455. [CrossRef]
132. Niida, K.; Green, D.H. Stability and chemical composition of pargasitic amphibole in MORB pyrolite under upper mantle conditions. *Contrib. Miner. Pet.* **1999**, *135*, 18–40. [CrossRef]
133. Mantisi, B.; Sator, N.; Guillot, B. Structure and transport at grain boundaries in polycrystalline olivine: An atomic-scale perspective. *Geochim. Cosmochim. Acta* **2017**, *219*, 160–176. [CrossRef]
134. Marquardt, K.; Faul, U.H. The structure and composition of olivine grain boundaries: 40 years of studies, status and current developments. *Phys. Chem. Miner.* **2018**, *45*, 139–172. [CrossRef]
135. Sommer, H.; Regenauer-Lieb, K.; Gasharova, B.; Siret, D. Grain boundaries: A possible water reservoir in the Earth's mantle? *Miner. Pet.* **2008**, *94*, 1–8. [CrossRef]

136. Demouchy, S. Diffusion of hydrogen in olivine grain boundaries and implications for the survival of water-rich zones in the Earth's mantle. *Earth Planet Sci. Lett.* **2010**, *295*, 305–313. [CrossRef]
137. Menegon, L.; Fusseis, F.; Stünitz, H.; Xiao, X. Creep cavitation bands control porosity and fluid flow in lower crustal shear zones. *Geology* **2015**, *43*, 227–230. [CrossRef]
138. Gilgannon, J.; Fusseis, F.; Menegon, L.; Regenauer-Lieb, K.; Buckman, J. Hierarchical creep cavity formation in an ultramylonite and implications for phase mixing. *Solid Earth* **2017**, *8*, 1193–1209. [CrossRef]
139. Précigout, J.; Prigent, C.; Palasse, L.; Pochon, A. Water pumping in mantle shear zones. *Nat. Commun.* **2017**, *8*, 15736. [CrossRef] [PubMed]
140. Précigout, J.; Stünitz, H.; Villeneuve, J. Excess water storage induced by viscous strain localization during high-pressure shear experiment. *Sci. Rep.* **2019**, *9*, 1–9. [CrossRef] [PubMed]
141. Green, H.W., II; Shi, F.; Bozhilov, K.; Xia, G.; Reches, A.Z. Phase transformation and nanometric flow cause extreme weakening during fault slip. *Nat. Geosci.* **2015**, *8*, 484. [CrossRef]
142. Incel, S.; Hilairet, N.; Labrousse, L.; John, T.; Deldicque, D.; Ferrand, T.P.; Wang, Y.; Renner, J.; Morales, L.; Schubnel, A. Laboratory earthquakes triggered during eclogitization of lawsonite-bearing blueschist. *Earth Planet Sci. Lett.* **2017**, *459*, 320–331. [CrossRef]
143. Thielmann, M. Grain size assisted thermal runaway as a nucleation mechanism for continental mantle earthquakes: Impact of complex rheologies. *Tectonophysics* **2018**, *746*, 611–623. [CrossRef]
144. Watson, E.B. Immobility of reduced carbon along grain boundaries in dunite. *Geophys. Res. Lett.* **1986**, *13*, 529–532. [CrossRef]
145. Duba, A.G.; Shankland, T.J. Free carbon, electrical conductivity in the Earth's mantle. *Geophys. Res. Lett.* **1982**, *9*, 1271–1274. [CrossRef]
146. Zhang, B.; Yoshino, T. Effect of graphite on the electrical conductivity of the lithospheric mantle. *Geochem. Geophys. Geosystems* **2017**, *18*, 23–40. [CrossRef]
147. White, R.S. The Earth's crust and lithosphere. *J. Petrol.* **1988**, 1–10. [CrossRef]
148. Artemieva, I.M. The continental lithosphere: Reconciling thermal, seismic, and petrologic data. *Lithos* **2009**, *109*, 23–46. [CrossRef]
149. Artemieva, I.M. *Lithosphere: An Interdisciplinary Approach*; Cambridge University Press: Cambridge, UK, 2011.
150. Yamauchi, H.; Takei, Y. Polycrystal anelasticity at near-solidus temperatures. *J. Geophys. Res. Solid Earth* **2016**, *121*, 7790–7820. [CrossRef]
151. Takei, Y. Experimental and theoretical approaches to grain boundary premelting: A possible origin of asthenosphere. *Geophys. Res. Abstr.* **2019**, *21*, 4687.
152. Jackson, J. Strength of the continental lithosphere: Time to abandon the jelly sandwich? *GSA Today* **2002**, *12*, 4–10. [CrossRef]
153. Ernst, W.G. Archean plate tectonics, rise of Proterozoic supercontinentality and onset of regional, episodic stagnant-lid behavior. *Gondwana Res.* **2009**, *15*, 243–253. [CrossRef]
154. Pilchin, A.N.; Eppelbaum, L.V. The early Earth and formation of the lithosphere. In *Book: The Lithosphere: Geochemistry, Geology and Geophysics*; Anderson, J.E., Coates, R.W., Eds.; Nova Science Publishers, Inc.: Hauppauge, NY, USA, 2008; pp. 1–68.
155. Van Hunen, J.; van den Berg, A.P. Plate tectonics on the early Earth: Limitations imposed by strength and buoyancy of subducted lithosphere. *Lithos* **2008**, *103*, 217–235. [CrossRef]
156. Capitanio, F.A.; Nebel, O.; Cawood, P.A.; Weinberg, R.F.; Clos, F. Lithosphere differentiation in the early Earth controls Archean tectonics. *Earth Planet Sci. Lett.* **2019**, *525*, 115755. [CrossRef]
157. Gerya, T. Geodynamics of the early Earth: Quest for the missing paradigm. *Geology* **2019**, *47*, 1006–1007. [CrossRef]
158. Kirdyashkin, A.A. Forces acting on a subducting oceanic plate. *Geotectonics* **2014**, *48*, 54–67. [CrossRef]
159. Selway, K. Negligible effect of hydrogen content on plate strength in East Africa. *Nat. Geosci.* **2015**, *8*, 543–546. [CrossRef]

160. Ye, G.; Unsworth, M.; Wei, W.; Jin, S.; Liu, Z. The lithospheric structure of the Solonker Suture Zone and adjacent areas: Crustal anisotropy revealed by a high-resolution magnetotelluric study. *J. Geophys. Res. Solid Earth* **2019**, *124*, 1142–1163. [CrossRef]